Global investigation of olivine on Mars: Insights into crust and mantle compositions

A. Ody,[1] F. Poulet,[1] J.-P. Bibring,[1] D. Loizeau,[2] J. Carter,[3] B. Gondet,[1] and Y. Langevin[1]

[1]   We present the distribution of olivine on Mars, derived from spectral parameters based on the 1 µm olivine absorption band. The olivine can be defined with respect to two spectral end-members: type 1 corresponds to olivine with low iron content and/or small grain size and/or small abundance, and type 2, which corresponds to olivine with higher iron content and/or larger grain size and/or larger abundance. The spatial and statistical analysis of the global olivine distribution points out five major geological settings where olivine is detected: (1) Early Hesperian olivine-bearing smooth crater floors and flat intercrater plains throughout the southern highlands; (2) olivine deposits around the three main basins Argyre, Hellas, and Isidis; (3) olivine in intercrater dunes, crater ejecta, or extended deposits in the northern plains; (4) olivine associated with outcrops and sand in the floor of Valles Marineris; and (5) olivine-bearing butte outcrops in the vicinity of Hellas. The geological context, the age, and the composition of the olivine detections associated with these five major geological settings are detailed. Their origin and the implication of their occurrence on the composition of the Martian mantle and crust, as well as on the evolution of Mars volcanism are discussed.

Citation: Ody, A., F. Poulet, J.-P. Bibring, D. Loizeau, J. Carter, B. Gondet, and Y. Langevin (2013), Global investigation of olivine on Mars: Insights into crust and mantle compositions, *J. Geophys. Res. Planets*, *118*, doi:10.1029/2012JE004149.

1.   Introduction

[2]   The processes responsible for the formation of the crust and of the upper mantle of a large planetary body can include the formation and the solidification of a magma ocean, the density stratification and overturn, large-scale convection, and volcanic activity [*Taylor and McLennan*, 2009]. These processes are expected to produce distinct mineral assemblages across its surface.

[3]   Compositional investigations of Mars with various remote sensing and in situ observations have revealed a wide diversity of igneous minerals [e.g., *Christensen et al.*, 2005; *McSween et al.*, 2009; *Poulet et al.*, 2007, 2009a, 2009b]. Among them, olivine is diagnostic of the petrologic evolution and history of mafic igneous rocks. Olivine is one of the first minerals to crystallize from a magma. Abundant olivine in a basaltic rock is usually an indication that the basaltic magma was mantle-derived and reached the surface without significant fractionation. For instance, *McSween et al.* [2006] concluded that the rocks at Gusev crater with high olivine abundance (~15–20%) are representative of primitive mantle magmas that were erupted on the surface as picritic basalts. However, the detection of olivine-bearing basaltic rocks can be misleading, because they may constitute fractionated basalts containing cumulus olivine. The composition of olivine is also a record of the degree of evolution of the source magma. Mg-rich olivine is for instance indicative of a relatively primitive source. The presence of olivine can thus be exploited to determine the origin and subsequent evolution of its parent magma.

[4]   Olivine-bearing exposures were detected on the surface of Mars by several works [*Hoefen et al.*, 2003; *Christensen et al.*, 2003, 2005; *Mustard et al.*, 2005; *Rogers et al.*, 2005; *Poulet et al.*, 2007; *Koeppen and Hamilton*, 2008; *Ody et al.*, 2012]. They were emplaced at various locations throughout the formation of the upper crust, with their growing inventory suggesting that ultramafic (picritic) materials may be relatively common. The distribution and the geological context of the olivine-bearing exposures on Mars are here investigated from data obtained from the near-infrared imaging spectrometer Observatoire pour la Minéralogie, l'Eau, les Glaces et l'Activité (OMEGA, on board the European Space Agency (ESA) Mars Express mission. Visible to near-infrared reflectance spectroscopy is sensitive to the presence of this mineral, because olivine reflectance spectrum is characterized by a composite absorption near 1 µm caused by crystal-field transitions in Fe^{2+} ions situated in distorted octahedral crystallographic sites [*Gaffey et al.*, 1993]. Absorption features shift in generally understood ways with changing major element (MgO and FeO) content, but grain size and abundance effects can complicate a lot the interpretations of olivine reflectance spectra and thus its composition [*Poulet et al.*, 2007].

---

[5] OMEGA-based global spatial distribution of various mineral species including olivine has been reported in a previous paper [*Ody et al.*, 2012]. Here we present the detailed analyses of the composition and of the complex and various geological settings of the olivine on Mars, inferred from OMEGA data using various approaches: spectral indexes, spectral modeling with a radiative scattering model, geomorphological studies at regional and local scales, crater-counting dating, relationships with other observational parameters, and comparison with other data sets.

[6] The areas in which olivine is identified are very diverse but large and well-defined geological settings are derived. Potential sources of the olivine-bearing material are then discussed for each major surface deposit.

2. Data Set and Olivine Detection Method

2.1. Data Sets

[7] The objective of this work is to constrain the nature and the origin of olivine-bearing terrains at a planetary scale by using near-infrared (NIR) hyperspectral imaging data. To do so, we chose a systematic approach to infer global-scaled trends in the distribution, compositional diversity, geomorphic context, and timing of the olivine exposures on Mars. The Compact Reconnaissance Imaging Spectrometer for Mars (CRISM, on board Mars Reconnaissance Orbiter) is surveying the Martian surface at very high spatial resolution but at the expense of a low coverage. Conversely, the lower spatial resolution instrument OMEGA achieved a complete survey of the surface during 3+ Martian years, making possible an investigation of the olivine signature at the global scale. We thus use OMEGA observations as the source of spectral data for this investigation.

[8] OMEGA consists of an infrared whisk-broom system coupled to a "visible" push-broom one, resulting in the measurement of surface radiance from 0.3 to 5.2 µm [*Bibring et al.*, 2004, 2005]. The footprint, proportional to the altitude of the spacecraft, ranges from 300 m to a few kilometers. This analysis focuses on NIR reflectance measurements using the "C channel" (spectral range 0.93–2.7 µm), covering the olivine 1 µm absorption band. All OMEGA data are systematically processed according to the standard data reduction schemes (irradiance and atmospheric absorption corrections) [*Bibring et al.*, 2005; *Langevin et al.*, 2007; *Ody et al.*; 2012] that produce reflectance I/F spectra. This study is based

on the final OMEGA C-channel data set, which corresponds to 3.6 Martian years, 8534 MEx orbits, 9628 three-dimensional image-cubes and more than 700 millions of pixels [*Ody et al.*, 2012]. In this large data set, surface frosts, atmospheric effects (clouds, aerosols), and instrumental artifacts, which interfere with surface observations, have been removed thanks to several automated filtering processes described in *Ody et al.* [2012].

[9] The detailed analysis of the olivine-bearing terrains with their detailed morphologic features, their stratigraphic relationships with their surrounding olivine-poor terrains, and their local-scale spatial distributions was performed to better constrain their formation processes and their origin. Detailed geomorphic analyses were supported by HiRISE images (High Resolution Imaging Science Experiment) [*McEwen et al.*, 2007] and a series of CTX mosaics (Context camera) [*Malin et al.*, 2007]. The Thermal Emission Imaging System (THEMIS) and Thermal Emission System (TES) were used to assess the thermo-physical properties. Approximate relative ages according to stratigraphic conventions summarized by *Tanaka et al.* [1992] are considered, but more precise dating measurements of specific regions were performed thanks to the HRSC (High Resolution Stereo Camera, *Jaumann et al.*, 2007) panchromatic images and CTX ones (section 4.1.2).

2.2. Olivine Identification and Composition

[10] The olivine detection is based on a spectral parameter approach presented in *Ody et al.* [2012] and summarized hereafter. The 1 µm complex olivine absorption band varies in depth, width, position, and shape with the iron content of the olivine, the grain size and the abundance of the olivine, making difficult to retrieve the real olivine composition [*Poulet et al.*, 2007]. Specifically, increasing the grain size broadens the bottom of the band and shifts its right wing toward longer wavelength, so that a Mg-rich olivine spectrum with very large grains ($>> 100\,\mu m$) and a Fe-rich olivine spectrum with smaller grains have similar spectral features hardly distinguishable in the NIR. The signature is also affected by the presence of other mineral species (pyroxene, dust), so that, for instance, a low abundance of Fe-rich olivine mixed with other minerals as pyroxene cannot be easily distinguished from a Mg-rich olivine. In order to identify, classify, and map the olivine signature, three spectral parameters have been implemented (Table 1).

Table 1. Description of Mapped Olivine Spectral Parameters[a] First Used by *Poulet et al.* [2007] and Adapted by *Ody et al.* [2012]

OSP1	$(0.5R(1.54) + 0.5R(1.56))/$ $(0.1R(1.01) + 0.2R(1.21) + 0.7^{a}R(1.36))$ before orbit 7768 $(0.5R(1.54) + 0.5R(1.56))/$ $(0.1R(1.03) + 0.2R(1.21) + 0.7^{a}R(1.36))$ after orbit 7768[b]	1.04	1 µm band due to olivine with a low iron content and/or a small grain size and/or a low abundance
OSP2	$(0.5R(1.69) + 0.5R(1.70))/$ $(0.05R(1.01) + 0.05R(1.21) + 0.45R(1.36) + 0.45R(1.5)$ before orbit 7768 $(0.5R(1.69) + 0.5R(1.70))/$ $(0.05R(1.03) + 0.05^{a}R(1.21) + 0.45R(1.36) + 0.45R(1.49)$ after orbit 7768[b]	1.04	1 µm band due to olivine with a higher iron content and/or a larger grain size and/or a higher abundance.
OSP3	$R(1.36)/(R(1.07)^{0.5a}R(1.64))^{0.5}$	Median (OSP3)-0.04	1 µm band due to olivine with a higher iron content and/or a larger grain size and/or a higher abundance.

[a]R is the reflectance I/F at a given wavelength λ (µm)/cos(i) with i as incidence angle relative to the aeroid.
[b]Spectel 6 (1.01 µm) and spectel 40 (1.5 µm) became nonfunctional after orbit 7768 due to cosmic ray degradations. They have been replaced by spectels 7 (1.03 µm) and 39 (1.49 µm) for evaluating OSP1 and OSP2 after this orbit.

The first spectral parameter (OSP1 in Table 1) detects Mg-rich and/or small grain-sized ($<<100\,\mu m$) and/or a low-abundance (about 10%) olivine. The second spectral parameter (OSP2 in Table 1) is more sensitive to olivine with higher iron content and/or larger grain size and/or at higher abundance. A threshold at a value of 1.04 is taken for both spectral parameters so as not to display false positives. *Poulet et al.* [2007] have demonstrated that this threshold allows detecting 5% (respectively 20%) or more of Mg-rich olivine with grain size of $100\,\mu m$ (respectively $10\,\mu m$) in a basaltic mixture. Because the increase of the iron content strongly favors the identification of the olivine by OMEGA, the iron-rich olivine can be detected in very small abundance (~5%) even for small grain size.

[11] An increase of the value of both olivine parameters can be interpreted as an increase of the iron content, and/or of the grain size and/or of the abundance. Examples of calculated values as a function of the spectral characteristics of olivine are listed in Figure 1. There is a range of OSP1 values (preferentially larger than ~1.08), for which OSP2 indicates also positive detections (with preferentially small OSP2 values). For very strong olivine signatures, the OSP1 value decreases because the continuum wavelength taken at about $1.5\,\mu m$ (Table 1) corresponds to the bottom of the $1\,\mu m$ olivine band for large grain size and/or iron content. This demonstrates that OSP1 can be used to map olivine with low abundance, low iron content, and small grain size, whereas OSP2 will preferentially map olivine with larger abundance and/or grain size and/or iron content.

[12] OSP3 measures the band depth centered at $1.36\,\mu m$ (Table 1). This band depth is then compared to its median value within a given image-cube, and only values 4% larger than the median are considered as valid detections. This procedure is well adapted to the typical small surface fraction of regions exhibiting olivine signatures and minimizes the impact of aerosol/dust cover contributions that bluish the spectral shape in increasing reflectance at low

wavelengths, as well as that of departures from linearity of the OMEGA detector (typically 1 to 2%, with variations in behavior from cube to cube). A comparison between the detections obtained by the three parameters shows that OSP3 and OSP2 detect similar spots. However, OSP3 has the advantage to detect olivine in terrains where OSP2 fails to do so because of the presence of aerosols and/or dust cover, whereas the OSP2 parameters detections are more robust when decreasing the threshold.

[13] The thresholds of each olivine parameter applied to derive the global olivine map are chosen to be restrictive to avoid any false positives and remove artifacts. However, visual inspections of some areas of deposits with values of olivine parameters below the nominal thresholds reveal the presence of olivine signature. This visual inspection is performed by applying the spectral ratio technique in which the spectrum of a region of interest is divided by the spectrum of a nearby region of low spectral contrast. This technique allows checking the presence of olivine signature of the region of interest by suppressing residual calibration artifacts, atmospheric effects or spatial mixture effects with other materials (pyroxene- and dust-bearing mobile material), which can partly modify or even mask the olivine signature. For a local study, the threshold of olivine parameters can thus be adapted to each observation. This value is defined thanks to a detailed spectroscopic analysis using spectral ratios to verify the mineral detection and detect boundaries of these olivine-bearing deposits. New olivine deposits that were not mapped or only partially on the global map, have hence been carefully identified for local- or regional-scale studies.

[14] For detailed analyses (section 4), the identification is performed by using the OSP2 spectral parameter only. This spectral parameter is more sensitive to the shape of the $1\,\mu m$ band than the OSP1 parameter, and thus decreasing its threshold presents less risk of detecting other minerals (pyroxene, crystalline ferric oxides). This parameter has also
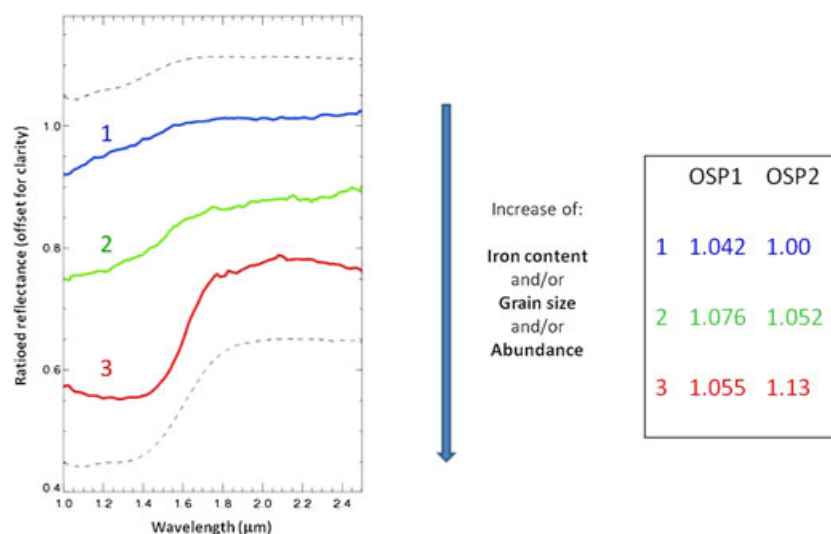
Figure 1. Examples of ratioed spectra extracted from three different regions of Mars and the corresponding values of OSP1 and OSP2. The variation of the signatures are interpreted as an increase of iron content, and/or grain size and/or abundance. The spectra are compared to RELAB laboratory spectra of fayalite (upper dotted line, "c3po59_bdvnir") and forsterite (bottom dotted line, "c3po53_bdvnir") with grain size between 45 and $70\,\mu m$.

the advantage of always increasing with the 1 µm band depth and width contrary to OSP1.

[15] Given the complexity of deriving olivine composition from NIR spectral signatures, indication on iron content, grain size, and abundance will be mainly obtained through type class signatures (see section 3.1). Nevertheless, a radiative transfer modeling will be applied for some deposits of interest to precise the iron content. This model based on the *Shkuratov et al.* [1999] theory and adapted to basaltic surfaces by *Poulet and Erard* [2004] allows inferring the modal abundance of surfaces by using a library of selected end-members. To reproduce a basaltic mixture spectra, pyroxenes (both low-calcium and high-calcium pyroxenes) and plagioclase are intimately mixed with olivine [*Poulet et al.*, 2009a, 2009b]. Three starting conditions were generally considered for each spectrum: one with a forsterite end-member alone with its grain size as a free parameter (modo 1), one with a fayalite end-member alone with its grain size as a free parameter (modo 2), and the third one with both fayalite and forsterite end-members but with grain size fixed at 100 µm (modo 3) to separate the grain size effect from the iron content. Grain size and abundances of other minerals are free parameters in all cases.

3. Global Distribution of Olivine

3.1. Olivine Mapping: Type 1 and Type 2 Spectra

[16] An olivine global map is built using all observations between −60° and +60° and a resolution of 40 pixels per degree (ppd), well adapted to the spatial sampling of OMEGA observations. This map is obtained by merging the three olivine spectral parameters as follows: all OSP1 values are first plotted from blue to green, then OSP3 in green and OSP2 from green to red (Figure 2). The color scale from blue to red is thus an indicator of the values of parameters and thus of the nature of the olivine as discussed previously. In order to exhibit detections that could be masked by lower quality overlapping observations (with lower resolution or disturbed by aerosols, icy frost, and clouds despite the filtering process), only the highest value of criteria for each pixel is plotted whenever there is an overlap. Olivine global map is overlain on Mars Orbiter Laser Altimeter (MOLA) map to better visualize the locations of the detections. The value of the spectral parameter for each pixel is recorded on ArcGIS and mapped with symbols larger than the size of an OMEGA pixel in order to make the detections more visible.

[17] Detections in blue emphasize weak olivine signatures identified with OSP1 and should correspond to Mg-rich and small grain size (<100 µm) and low abundance. The olivine identified in blue is defined as Type 1 olivine. Detections mapped in red have the strongest signatures observed by OMEGA and correspond to olivine with highest iron content, and/or largest grain size (> > 100 µm) and/or highest abundance (>25%). Green detections mainly correspond to olivine spots detected with the three parameters and with respectively high OSP1 values (>1.08) and small/medium OSP2 values and all OSP3 values. They are interpreted to have intermediate compositions/abundances/grain sizes. Both red and green detections are grouped into a new type of olivine, defined as Type 2 olivine. Typical end-members are located in Terra Tyrrhena for the blue detection, circum-Argyre for the green one and Nili Fossae

for the red one. Their corresponding spectra are shown in Figure 1.

[18] This mapping method allows to highlight regions with relatively high olivine abundance in comparison to the mean Martian surface composition and to reveal their diversity in term of iron content, grain size and abundance. However, as previously mentioned, we cannot totally exclude that some areas below the detection thresholds may contain a certain amount of olivine, which can reach up to 15% of pure forsterite with small grain size (10 µm or less) mixed with other basaltic minerals.

3.2. Global Analysis

[19] The olivine global map presented in Figure 2a shows that olivine is mostly located in the ancient southern highlands with some localized spots scattered in the northern plains. All previously identified large olivine regions including Nili Fossae, Terra Tyrrhena, Chryse Planitia, Argyre basin, Valles Marineris are visible [e.g., *Bandfield*, 2002; *Christensen et al.*, 2003; *Hoefen et al.*, 2003; *McSween et al.*, 2006; *Hamilton and Christensen*, 2005; *Mustard et al.*, 2005; *Poulet et al.*, 2007; *Koeppen and Hamilton*, 2008; *Edwards et al.*, 2008; *Salvatore et al.*, 2010; *Rogers and Fergason*, 2011; *Loizeau et al.*, 2012]. Most of the Type 1 olivine deposits occur in broad low albedo southern terrains with uneven spatial distribution. Several regions exhibit a larger number of occurrences: Terra Cimmeria, Terra Sirenum, Sinus Meridiani, regions between Argyre and Valles Marineris and between Terra Sabaea and Hesperia Planum including Terra Tyrrhena. Some other deposits are also observed in the volcanic provinces of Syrtis Major, Thaumasia Planum and Hesperia Planum. Although Type 2 olivine is also visible in these Type 1 deposits, it commonly occurs as more discrete occurrences (several pixels to a few tens of pixels across) scattered over the Martian surface except around the three main basins Argyre, Hellas, and Isidis where larger concentrations of occurrences are present. Olivine is also detected within the northern plains mainly associated with crater ejecta and dunes on crater floors as previously reported by *Bibring et al.* [2005]. Numerous additional detections are visible here in the region of Utopia Planitia.

[20] This uneven olivine distribution is well correlated to low-dust and pyroxene-bearing regions. A comparison of the olivine distribution with the OMEGA-based global distribution of pyroxene as mapped by *Ody et al.* [2012] indicates that olivine detections are indeed typically associated with pyroxene-rich regions. On Figure 3, we filtered olivine detections in removing all pixels with positive detections of pyroxene. These "pyroxene-free" olivine spots appear to be rather similar to those mapped in green and red on Figure 2 (olivine Type 2 distribution), with detections mainly found in the region of Nili Fossae, Argyre, and Hellas terraces and in the northern plains. Some occurrences are also detected in Valles Marineris as well as in the southern highlands mainly associated with crater floors. The only widespread deposit of Type 1 is found in Terra Meridiani. This detection is in good agreement with the minor amount of olivine without pyroxene signature reported in the unit Ph (hematite-bearing plains [*Poulet et al.*, 2008]).
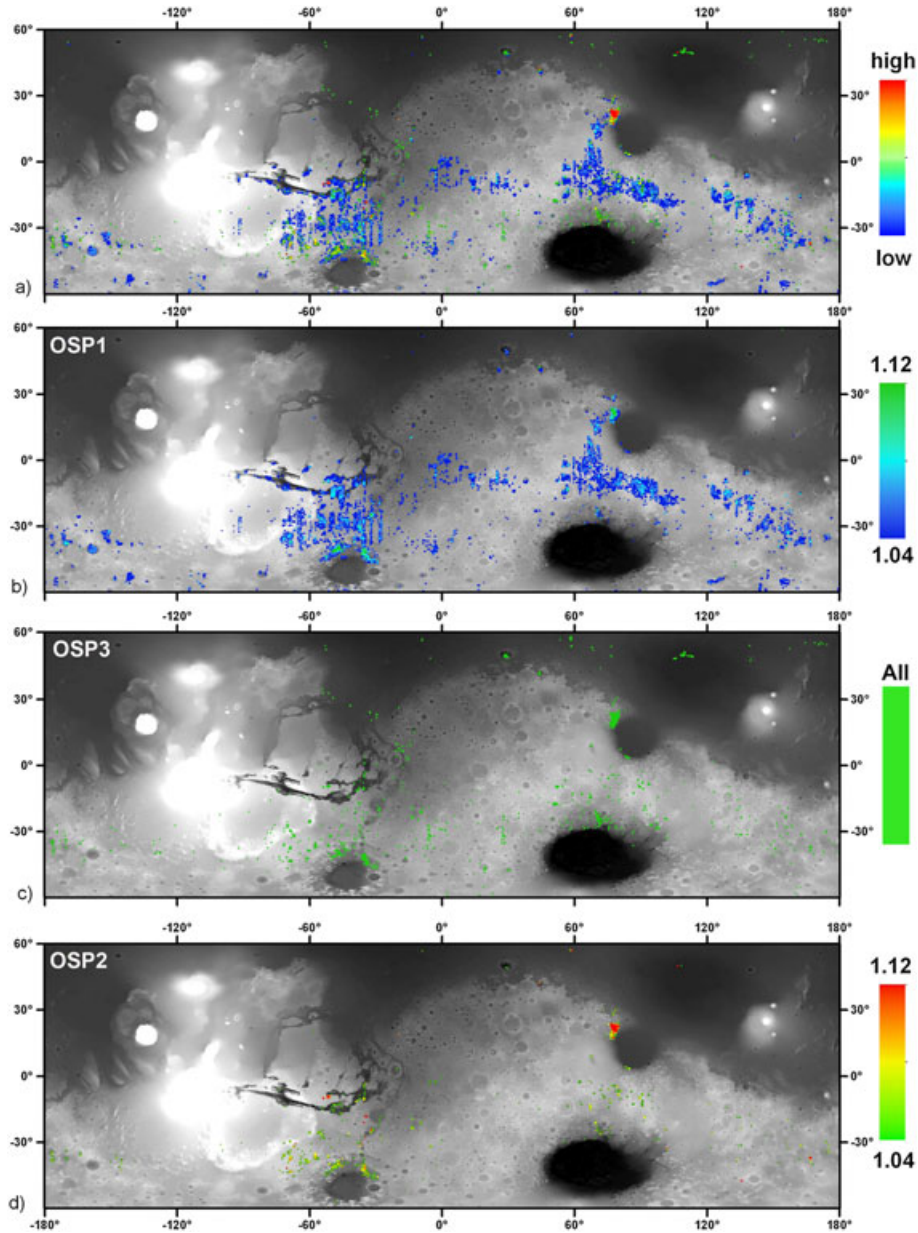
Figure 2. (a) Olivine global map obtained by merging the three spectral parameter maps (Figures 2b, 2c, and 2d) as follows: all OSP1 (b) values are first plotted from blue to green, then OSP3 (c) in green and OSP2 (d) from green to red. Color scale from blue to red can be interpreted in terms of low to high iron content and/or grain size and/or abundance (see text); spots are larger than actual sizes, for visibility.

3.3. Distribution with Elevation and Latitude

[21] We binned all pixels presenting positive olivine detection (at least one of the three spectral parameters larger than its threshold) as a function of elevation to look for any trend(s) in global topography and/or stratigraphy. To avoid areal biases, we normalized each 100 m elevation bin by the total number of global map pixels at this bin elevation. The resulting histogram represents the percentages of pixels with positive olivine detection for each bin altitude with respect to the total number of pixels at this bin altitude (Figure 4A). The olivine distribution with elevation is distributed in four distinct intervals of elevation: (a) the 0 to 3 km interval primarily includes olivine spots widespread throughout the southern highlands; (b) olivine in the 0 to –2.5 km range is associated with spots in the terraces of the three main basins, Terra Meridiani and some large and deep craters of the southern highlands; (c) the peak of olivine detections between –2.5 and –5 km primarily corresponds to olivine detected in the floor of Valles Marineris, in the inner rims of Isidis and Hellas and detections in the Northern plains; (d) finally, the interval between –5 and –7 km corresponds to olivine associated with dunes on deep crater floors of the northern plains. The regions defined by these four intervals can be seen on Figure 4C where olivine detections are superimposed on MOLA map.
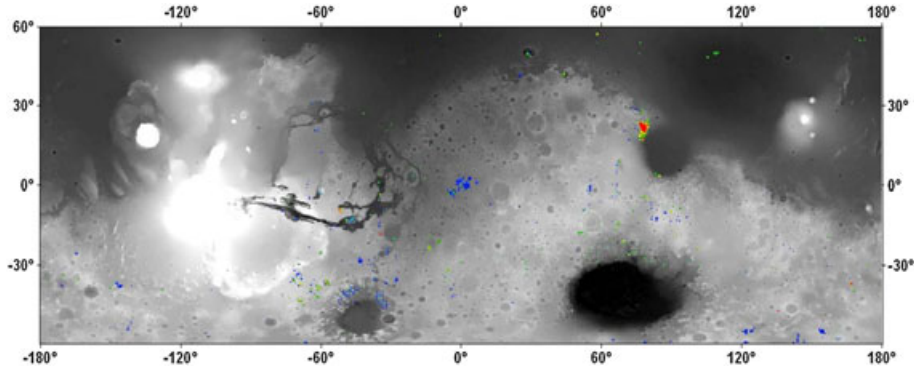
Figure 3. Pyroxene-free olivine distribution. All pixels with positive detection of pyroxene based on its 2 μm band [Ody *et al*., 2012] are not plotted. The color scale is the same as in Figure 2.
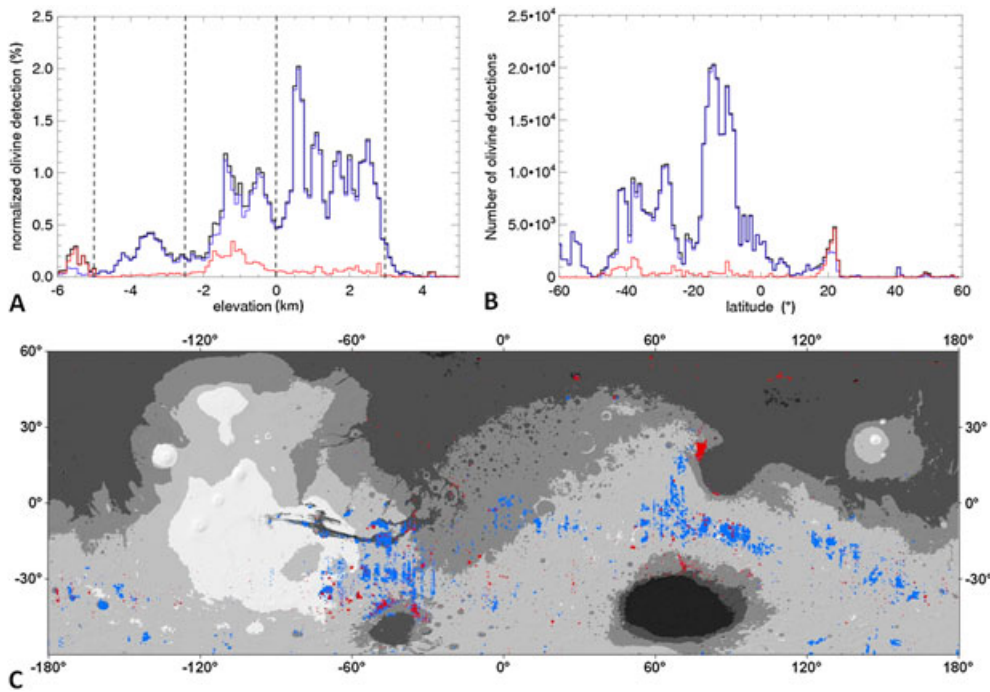
Figure 4. (A) Density of mapped pixels binned by 100 m for all olivine spots (black line), Type 1 olivine spots (blue) and Type 2 olivine spots (red). Dashed lines indicate the four major intervals of elevation. (B) Olivine detections as a function of latitude (black: all olivine pixels, blue: Type 1 olivine, red: Type 2 olivine) (C) Distribution of Type 1 (blue) and Type 2 (red) olivine over MOLA altimetry map separated in five altimetry intervals: black regions: [< –5 km]; dark gray: [–5; –2.5 km]; gray: [–2.5; 0 km]; white gray: [0; 3 km]; white: [> 3 km].

[22] Interestingly, olivine in the broad [–5, –2.5 km] elevation range has a peak at –3600 m, which is close to the olivine elevation enhancement derived from TES data [*Edwards and Christensen*, 2011]. The OMEGA-based distribution centered at this peak is nevertheless much broader than the relatively narrow –3900 to –3600 m TES-based elevation range. The enhancements are primarily attributed to deposits located in Valles Marineris. Although less numerous, occurrences located in the region Chryse Planitia are also a part of this interval. At this stage, it is difficult to tell if this elevation interval represents a large (regional) horizontal and vertical scale olivine-bearing layer or merely the region where olivine is most commonly exposed due to recent erosion and excavation processes.

[23] Another representation of the elevation relationship is to separate the two types of olivine with histograms in blue and red corresponding to Type 1 (OSP1 greater than its threshold and OSP2 and OSP3 lower than their threshold) and Type 2, respectively (Figure 4A). Their respective spatial distribution is illustrated in Figure 4C by using the same color code. Most of olivine detected in the [0, 3 km] range has a Type 1 olivine composition, whereas some localized exposures of Type 2 olivine are barely visible in these terrains. The terraces of the two main basins Hellas

and Argyre as well as Nili Fossae region [–2.5, 0 km] exhibit numerous Type 2 olivine spots. Olivine in Valles Marineris [–5, –2.5 km] is dominated by olivine type 1 with some occurrence of olivine type 2. Olivine in the northern plains [–7, –2.5 km] is spectrally dominated by Type 2 and primarily identified by OSP3 because of disturbing atmospheric and surface conditions.

[24] We binned the detections as a function of latitude to search for potential influence of climate, dust, or geological structures (Figure 4B). Olivine is mostly common between 10°N and 60°S in the dust-free highlands. Type 1 olivine present in the southern highlands is distributed along three ranges of latitudes: the 10°N to 25°S range includes the regions of Terra Tyrrhena and Valles Marineris; the second interval between 25°S and 50°S groups together the detections found in the North and West of Argyre, the Hellas and Argyre basin rims, and some detections in Terra Sirenum and Terra Cimmeria. The third interval is located between 50°S and 60°S including large deposits south of Terra Cimmera and Terra Sirenum. The peak centered at 22°N corresponds to Nili Fossae region that includes the majority of Type 2 olivine detections. The rest of the olivine Type 2 is identified in more discrete occurrences throughout the southern highlands between 10°N and 50°S as well as in very localized spots in the northern plains [40°N, 60°N], as already mentioned with the elevation histogram.

[25] No trend with latitude is observed, given that olivine is mostly located between 10°N and 60°S; the latitude histograms of olivine merely represent the latitudes of main deposits. The gap between 45°S and 55°S is mainly due to the geological structures (floors of Hellas and Argyre) as well as to a presence of widespread dusty regions in East and West of Hellas basin between 30°E and 180°E and in Terra Sirenum. Away from this dusty region, olivine is clearly detected in the low albedo terrains of this latitude range. Spectral analysis of OMEGA data identifies olivine (and pyroxene) in the high southern latitudes regions of the circum-Hellas volcanic province [*Williams et al.*, 2010]. The polarward regions, which are characterized by stronger and various seasonal processes of sublimation/condensation of ices and major condensation of water vapor that could favor chemical and/or mechanical weathering and thus alteration of olivine exhibit also the presence of this mineral [*Poulet et al.*, 2008; *Carrozzo et al.*, 2012; *Ody et al.*, 2012]. The global, large-scale distribution of olivine appears thus to be mainly controlled by the presence of dust rather than any other effect.

3.4. Distribution With Thermal Inertia

[26] We now investigate the near-surface physical properties of the olivine deposits material by comparing our olivine map with the 20 pixels/degree TES thermal inertia (TI) map [*Putzig and Mellon*, 2007]. Thermal inertia is a measure of the subsurface's ability to store heat during the day and to reradiate it at night. From orbit, thermal inertia depends on a complex combination of particle size, rock abundance, and the degree of induration of the observed surface material. However, although abundant rock and bedrock do have the effect of slightly raising the thermal inertia in the field of view, the effects of the fine material at the surface are primarily distinguished [*Christensen*, 1986]. Typically, low thermal inertia between 5 to about 150 J m^{-2} K^{-1} s$^{-1/2}$

(tiu hereafter) represent loose fine-grained material (dust) with no or a very few rock [*Mellon et al.*, 2000]. Higher thermal inertia have been interpreted as possibly representing more abundant surface rocks or bedrocks exposures, larger particles sizes, and/or more indurated fines forming a duricrust [*Kieffer et al.*, 1977; *Palluconi and Kieffer*, 1981; *Christensen*, 1986; *Jakosky and Christensen*, 1986; *Christensen and Moore*, 1992]. A surface is considered to be dominated by solid rock for a thermal inertia typically larger than 1200 tiu [*Edwards et al.*, 2009].

[27] The TES Thermal inertia map was resampled to the OMEGA olivine map resolution of 40 pixels/degree. Normalized histograms, representing the percentage of detections in each thermal inertia bin with respect to the total number of detections of the studied distribution, were constructed (Figure 5). For comparison, thermal inertia normalized histograms for the entire Martian surface and for pyroxene-bearing olivine-free regions are also plotted.
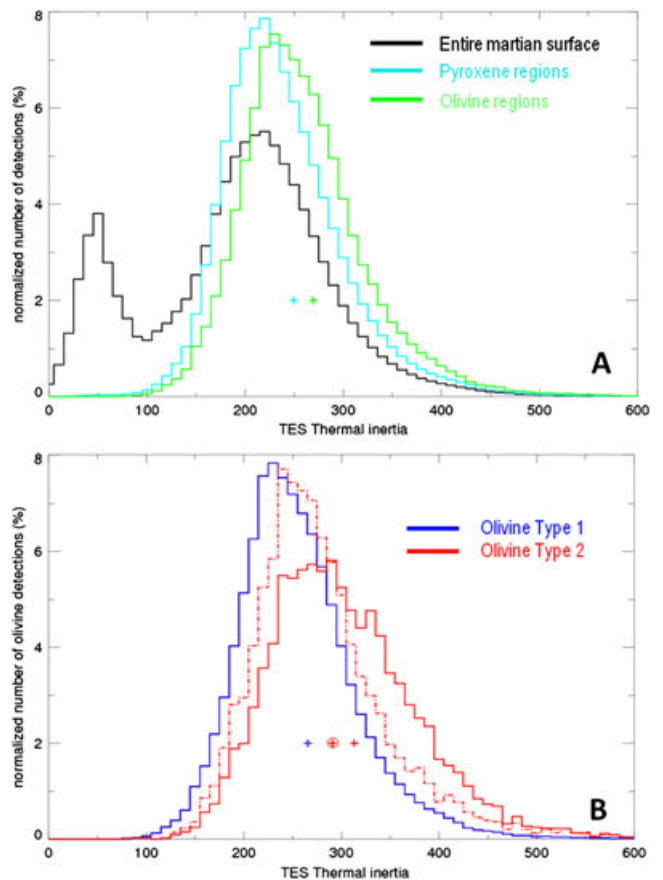
Figure 5. Normalized histograms comparing the mean thermal inertia of various terrains. These histograms represent the percentage of detections in each thermal inertia bin with respect to the total number of detections of the studied distribution (entire Martian surface, pyroxene regions, olivine regions (total, Type 1, Type 2, etc...)). (A) The mean values of thermal inertia for pyroxene-bearing olivine-free regions (250 +/– 67 tiu) and olivine-bearing regions (269 +/– 69) are indicated with crosses. (B) Same as Figure 5A but for Type 1 olivine regions (266 +/– 66, blue cross), Type 2 (313 +/– 81, red cross) and Type 2 without Nili Fossae detections (291 +/– 80, dashed line and red cross encircled).

Olivine-bearing thermal inertia ranges from ~100 to 600 tiu with most detections between 200 and 300 tiu. These values are typical of Martian low albedo mafic regions and consistent with sandy soils [*Fergason et al.*, 2006]. Values of ~300–600 tiu that represent 25% of the olivine detection can be extrapolated to millimeter-sized grain assuming a uniform particle size [*Pelkey et al.*, 2001]. Olivine thermal inertia distribution is slightly shifted to higher thermal inertia with respect to those of pyroxene-rich olivine-free regions (respectively 250 +/– 67 tiu in average for pyroxene-rich regions and 269 +/– 69 tiu for olivine-bearing regions). This difference of ~20 tiu is statistically not significant, although several studies report that olivine signatures are commonly associated with high thermal inertia surface [*Bandfield et al.*, 2011; *Bandfield and Rogers*, 2008; *Edwards et al.*, 2008; *Rogers et al.*, 2009; *Rogers and Fergason*, 2011]. OMEGA nevertheless detects olivine in terrains with very large values of thermal inertia (>1200 tiu) as already reported by previous studies using TES and THEMIS data sets [e.g., *Edwards et al.*, 2009], but these detections represent only several tens of pixels localized in Argyre rim and Valles Marineris. There is no strong evidence for a global relationship between olivine signature strength and high TI, and thus for potential mechanical and/or chemical weathering of bedrock outcrops as the prime driver of the olivine distribution. We thus consider at this point that the comparison at global scale is not sufficient and more detailed studies at local scale are necessary to better understand the properties and the relationships between the olivine-bearing and the olivine-poor terrains as also pointed out by *Hamilton et al.* [2010].

[28] The difference between Type 1 (blue histogram) and Type 2 (red histogram) olivine is illustrated in Figure 5B. Type 2 olivine is more typically found in higher thermal inertia surface. Because a significant number of Type 2 olivine spots is found in the Nili Fossae region, we have removed them in order to show the thermal inertia distribution of other Type 2 spots (residual histogram are shown in red dotted line on Figure 5B). The comparison between both histograms indicates that most of the Type 2 olivine detections with a high thermal inertia correspond to the region of Nili Fossae. Residual distribution of Type 2 olivine is then much more similar to the Type 1 olivine distribution although still slightly shifted to higher thermal inertia by 25 tiu. This small shift can provide insights about the difference between the Type 1 and Type 2 olivine as discussed below.

[29] A larger grain size for Type 2 olivine terrains would explain both higher thermal inertia and stronger signatures. However, this difference of 25 tiu is pretty small. Using the relationship between thermal inertia and grain size defined by *Pelkey et al.,* [2001], a 25 tiu (from 266 to 291 tiu) difference can be extrapolated to a variation of the grain size from ~500 μm to ~700 μm, which cannot explain the significant spectral signature between Type 1 and Type 2. We thus consider that a grain size effect cannot be responsible of the difference of 1 μm band strength and shape between the two types of olivine.

[30] Locally, a thin layer (<10 μm) of dust-bearing and/or pyroxene-bearing particles could both significantly reduce the Type 2 olivine signature and decrease the thermal inertia. We recall that most of the Type 1 olivine is located in the pyroxene-bearing regions of Mars where mobile material can partly cover the olivine-bearing deposits, and thus transform Type 2 signature to Type 1 signature. The heterogeneous presence of such a mobile material partial layer could thus satisfactorily explain the variation of olivine signature and thermal inertia observed in the same geological unit (see section 4.1).

[31] Conversely, the presence of a layer of mobile material can hardly explain the correlation between olivine type and large-scale and well-defined geographies, elevations, and morphologies. The variations of the olivine signature observed across the Martian surface could rather result from a difference in iron content or abundance. Modeling the abundance of olivine requires radiative transfer modeling as described in *Poulet et al.* [2009a]. This will be investigated in section 4 for some selected regions of interest. At this point, we thus consider that a difference in iron content and/or abundance is a likely explanation for the difference in olivine type between large-scale units.

3.5. Summary and Comparison With Other Data Sets

[32] The shape of the olivine 1 μm absorption band does not merely translate varying iron content. Grain size, abundance, and/or spectral mixture can also affect the olivine spectral shape making a fayalite-like spectrum similar to a forsterite-like spectrum and vice versa. As an example, the region of Nili Fossae that shows the most fayalite-like spectrum needs forsterite with large grain size and fayalite to be modeled by radiative transfer model [*Poulet et al.*, 2009b]. This global analysis has shown that the olivine detection can be referred to two end-member compositions based on their spectral shape: Type 1 olivine should correspond to Mg-rich and small grain size and low abundance olivine composition; Type 2 corresponds to olivine with higher iron content and/or larger grain size and/or larger abundance.

[33] The olivine detection map and our analysis of the distribution of olivine deposits as a function of elevation and latitude reveal that these deposits are distributed along five distinct geological settings: (1) the southern highlands with both olivine compositions. Type 1 olivine is found in extended deposits primarily located in the regions of Terra Cimmeria, Terra Sirenum, Sinus Meridiani, regions between Argyre and Valles Marineris and between Terra Sabaea and Hesperia Planum including terra Tyrrhena. Type 2 olivine is also found in these regions but in smaller and more discrete occurrences; (2) the circum-Argyre, -Hellas, and -Isidis basins with numerous Type 2 olivine occurrences; (3) the northern plains where olivine is primarily associated with craters (ejecta and dunes accumulated on floors), but also to extended deposits in Utopia Planitia; (4) Valles Marineris with a majority of olivine with Type 1 composition but with some exposures of strong olivine signature of Type 2 composition; and (5) other isolated, kilometer-sized spots and barely visible on the global map and preferentially of Type 2.

[34] Olivine on the surface of Mars was also inferred from TES data [*McSween et al.*, 2006; *Koeppen and Hamilton*, 2008]. The TES global distribution of olivine matches well with the distribution of Type 2 olivine in regions where strong signatures are reported (Nili Fossae, circum-Argyre and -Hellas, Valles Marineris). Whereas the TES olivine map shows detectable amounts of olivine (5–15 vol %) in

broad near-equatorial regions, the OMEGA-based distribution is much more spatially heterogeneous with numerous discrete occurrences rather than uniform and continuous enhancements of olivine. As a result, the OMEGA and TES distributions as a function of elevation and latitude are significantly different. However, it is important to note that broad regions with reliable TES detections (olivine abundance above 10%) are well consistent with the extensive olivine-bearing regions detected by OMEGA (Terra Tyrrhena, Cimmeria, Sirenum, region between Argyre and Valles Marineris, Sinus Meridiani).

[35] The elevation and latitude histograms merely represent the characteristics of the major geological settings. The major effect that controls the global, large-scale distribution of surface olivine seems to be the dust coverage. Thermal inertia analysis of these deposits indicates a global trend with olivine-bearing terrains having a slightly higher but not significant thermal inertia on average than the olivine-poor surroundings. The difference in thermal inertia between Type 1 and Type 2 cannot be attributed to a grain size effect. At a local scale, this difference could be attributed to the presence of a dust-bearing and/or pyroxene-bearing particles layer over the olivine deposits. However, this does not account for the difference in olivine type between large-scale units, which is thus attributed to either the iron content and/or the olivine abundance.

4. Detailed Analysis of Olivine Deposits

[36] The different geological regions studied here in detail are shown on Figure 6a. They correspond to the major olivine settings previously recognized. It is important to note that this study is note exhaustive but statistically meaningful. In the southern highlands, olivine deposits are found in Hesperian flat and extended plains (pink squares), in olivine-bearing Hesperian smooth crater floors (red filled circles), and associated with crater ejecta (yellow filled circles). Some olivine-bearing butte outcrops (purple stars) are also studied. In the northern plains, olivine is mainly found in dunes on crater floors (light blue filled circles), crater ejecta (yellow filled circles), and extended deposits (green stars). Olivine detected on basin terraces and in Valles Marineris is clearly visible on the olivine global map, so that no specific symbol is plotted to identify these deposits. In addition to the geological properties, investigations of the composition is based on Type 1 and Type 2 classification, except for the circum-basins deposits, whom their composition especially in terms of iron content is
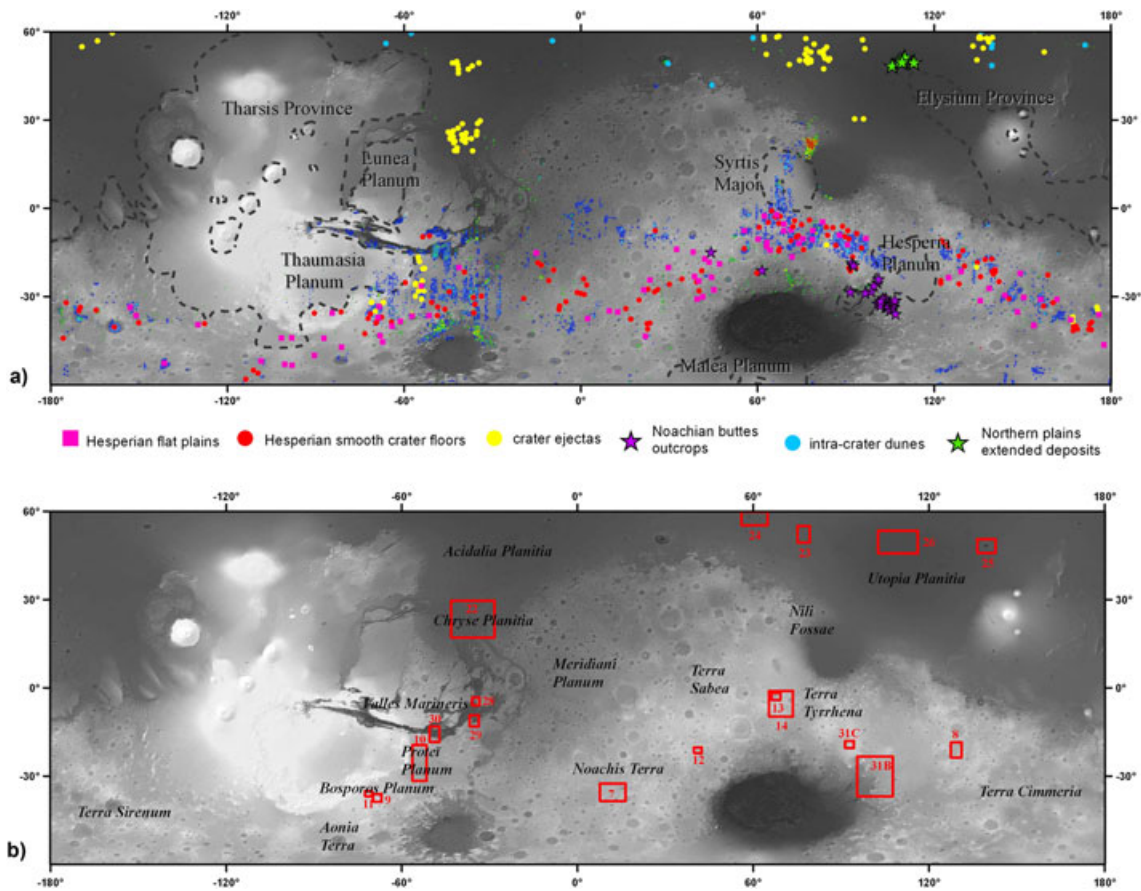
Figure 6. (A) Location of the olivine-bearing regions studied in details: Hesperian flat plains, Hesperian smooth crater floors, crater ejecta, Noachian buttes outcrops, dunes on crater floors, northern plain extended deposits, superimposed on a combined MOLA shaded-relief map and olivine map. The main volcanic provinces as mapped by *Werner* [2009] are outlined with dashed line. (B) Locations of the figures shown in the paper and labeled regions. Spectra extracted from each setting illustrated on these figures are shown in the Supporting Information.

mandatory to better constrain the implications. Examples of spectra extracted from each of these settings are available in the Supporting Information.

## 4.1. Extended Hesperian Olivine Deposits in the Southern Highlands

4.1.1. Settings

[37] Local-scale analysis of the widespread olivine-bearing deposits in the southern highlands has shown that olivine is mainly detected associated with smooth crater floor and flat intercrater plains that are commonly geographically associated. They are identified throughout the southern highlands, primarily in regions previously listed as pyroxene-rich dust-free regions (see section 3.1). Additional smooth crater floor and flat plains were identified in more dusty regions such as Noachis Terra and Aonia Terra by decreasing the olivine spectral parameter threshold. Olivine is also detected in small crater ejecta mainly localized in the region of Bosporos Planum, Protei Planum, and Terra Cimmeria and always associated with flat plains unit exhibiting weak or no olivine signature. No clear evidence of relationship between smooth crater floor or flat plains and major volcanic provinces as mapped by *Werner* [2009] are visible.

[38] Examples of OMEGA observations of four olivine-bearing flat plains are presented on Figures 7–10. These plains are commonly associated with flat plains units (Hpl3, Hplm) (Figures 7 and 9) or with ridged plains (Hr) (Figures 8 and 10) [*Skinner et al.*, 2006]. Some of these extended deposits are also found in Noachian mapped terrains [*Skinner et al.*, 2006]. However, all the olivine deposits are less cratered than their surrounding high-standing degraded terrains, and they embay them in some areas. They are well characterized on THEMIS daytime images by lower temperature with respect to adjacent terrains. This low daytime temperature is consistent with the higher nighttime temperature in THEMIS data resulting from higher thermal inertia than their surroundings. This higher thermal inertia is consistent with the rough and pitted texture, and little to no aeolian material seen on Figures 7E and 8D. This texture is commonly observed throughout the southern highlands but also in Eos Chasma, Ares Vallis, Gusev crater, and south of Isidis Basin [*Edwards et al.*, 2008; *Rogers et al.*, 2005; *Ruff et al.*, 2007; *Tornabene et al.*, 2008; *Rogers and Fergason*, 2011; *Edwards et al.*, 2009].

[39] In these flat plains, olivine signature usually increases on the nighttime higher-temperature regions. Small variations of the nighttime temperature are observed within the olivine plain units and could indicate difference in surface erosion and/or the presence of unconsolidated covering material which could originate from the olivine-poor surrounding terrains. In some plains, the highest olivine signatures are however correlated to the lowest nighttime temperature regions (Figure 9). This implies that olivine is present in less consolidated or finer-grained material, which is supported by the presence of ripple dunes on the surface, likely the result of in situ formation from the product of erosion of the underlying olivine-bearing bedrock (Figure 9D). This example demonstrates, first that olivine-bearing material is not found mainly in high thermal inertia terrains as suggested by *Bandfield et al.* [2011], and second, that sandy/silty soils on Mars are not necessarily olivine-poor relative to adjacent rocks or rocky surfaces that are likely the source for the soils. Similar conclusions were reached by *Hamilton*
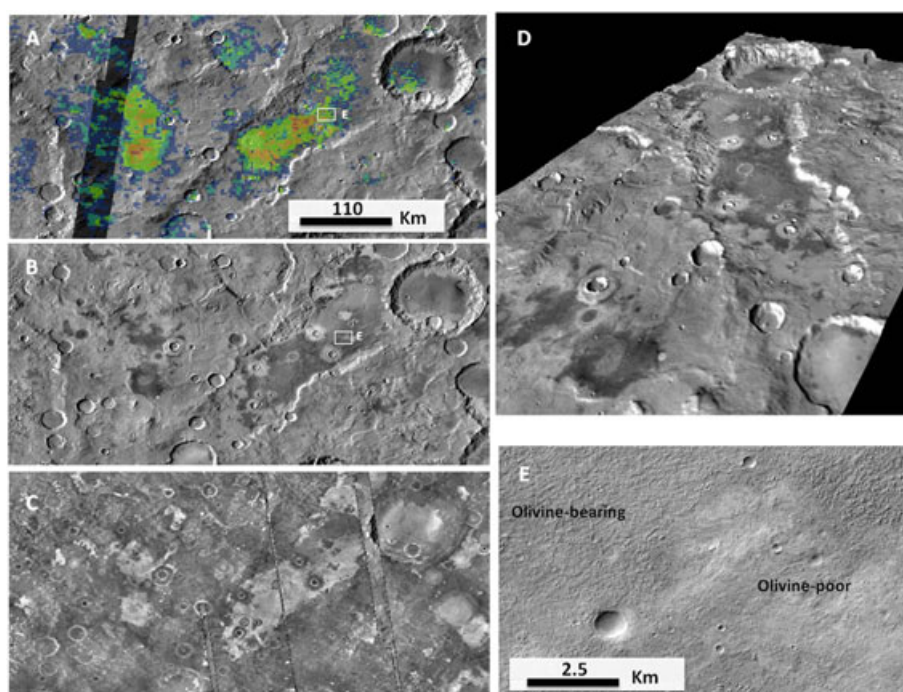

Figure 7. Example of flat Hesperian olivine-bearing flat plain and crater floors in the southern highlands [12.55°E, 35.4°S]. (A) Olivine map (OSP2 from 0.98 to 1.0); (B) Daytime THEMIS IR mosaic; (C) Nighttime THEMIS IR mosaic; (D) Three-dimensional (3-D) view of the area with a vertical exaggeration of 5; (E) CTX close-up illustrating the transition between olivine-bearing terrain and olivine-poor one (CTX_ID B17_016116_1456_XN_34S346W).
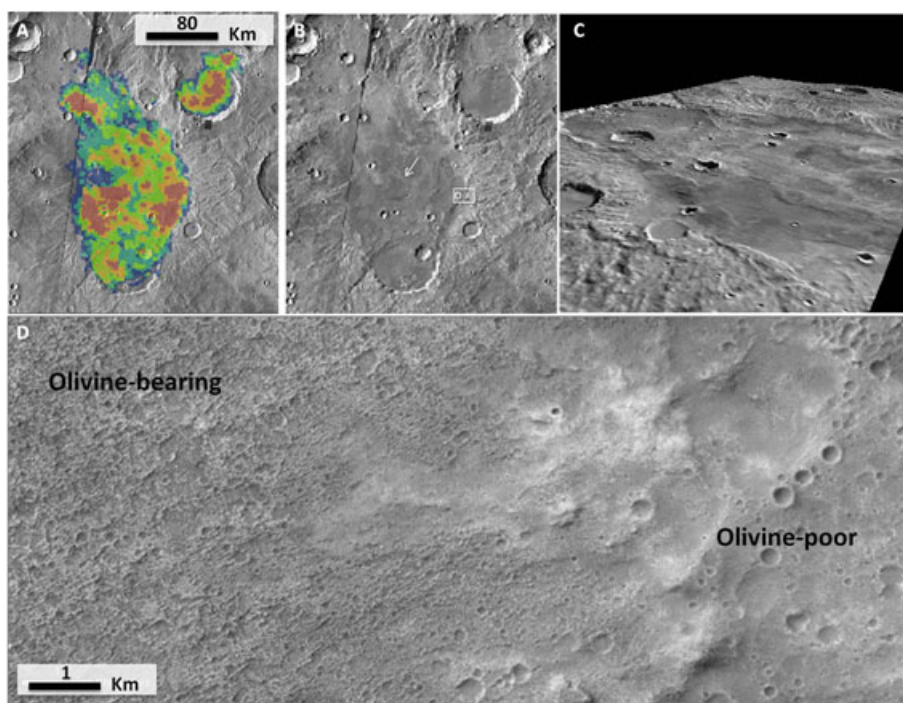
Figure 8. Example of olivine-bearing intercrater ridged plains and crater floors in the southern highlands [128.9°E, 21.6°S]. (A) Olivine map (OSP2 from 0.98 to 1.0); (B) Daytime THEMIS IR mosaic; (C) 3-D view of the area with a vertical exaggeration of 5; (D) CTX close-up illustrating the transition between the olivine-bearing terrain and the olivine-poor one. The white arrow indicates the presence of a ridge (CTX_ID P13_006262_1589_XN_21S230W).
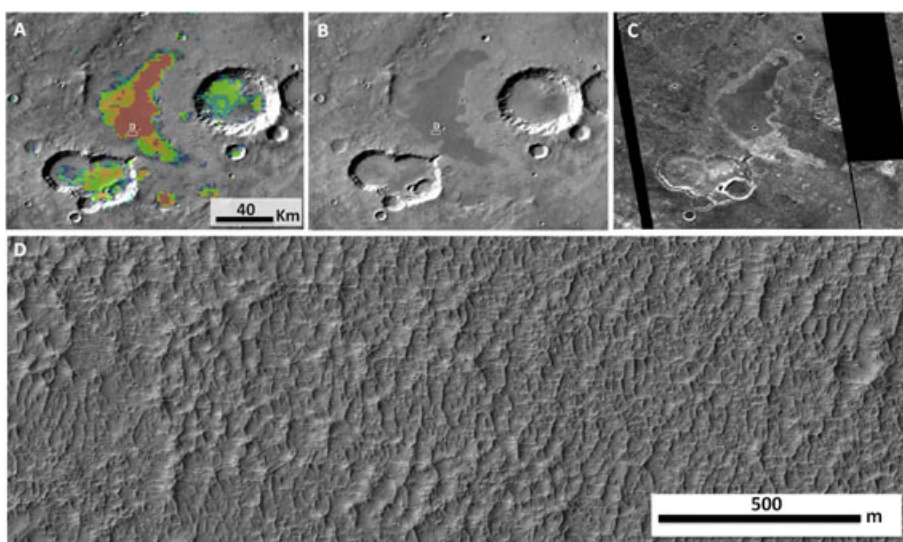

Figure 9. Example of olivine-bearing flat plain with low thermal inertia located at [291.2°E, 37.2°S]. (A) Olivine map (OSP2 from 0.99 to 1.05) over THEMIS IR daytime mosaic; (B) Daytime THEMIS IR mosaic; (C) Nightime THEMIS IR mosaic; (D) HiRISE detail on the low thermal inertia, olivine-bearing terrain (HiRISE_ID PSP_010739_1420).

et al. [2010] from TES data set. The fact that olivine signature is higher in sand than in bedrock could be explained by the mechanical segregation of olivine in sand as it is observed in Iceland [*Mangold et al.*, 2011].

[40] Olivine is not always detected in the entire flat ridged plain units. Figure 10 shows an example of large ridged plains centered at [−54°E, 23°S] where olivine is confidently identified only in small high nighttime (and low daytime) temperature regions of the ridged plain. Other parts of the ridged plain exhibit weak or inexistent olivine signature and have similar thermal properties than the Noachian surrounding terrains. CTX imagery shows that
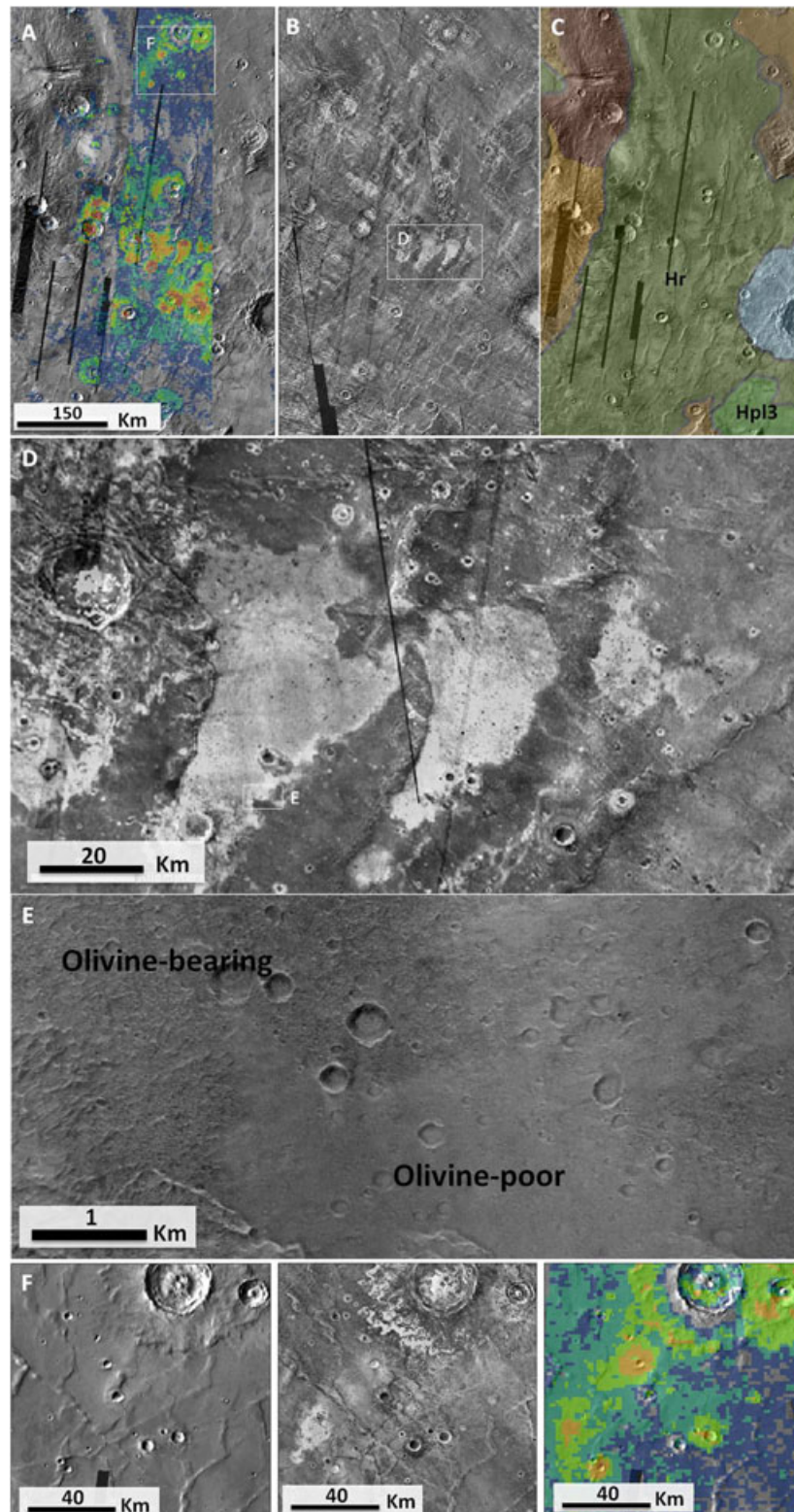
Figure 10. Ridged plains exhibiting variations of the olivine signature centered in [−54.1°E, 23.4°S]. (A) Olivine map (OSP2 from 0.99 to 1.04) over THEMIS IR daytime mosaic. (B) THEMIS IR nighttime mosaic. (C) U.S. Geological Survey (USGS) Geological unit (green: (Hr) Hesperian ridged plains; (Hpl3) Hesperian smooth unit; brown: Noachian units; grey: impact crater material [*Skinner et al.*, 2006]). (D) Close-up on the nighttime THEMIS IR mosaic. (E) CTX close-up of the boundary between olivine-bearing and olivine-poor terrains (CTX_ID P11_005504_1526_XN_27S054W). (F) From left to right, THEMIS IR daytime mosaic, THEMIS IR nighttime mosaic, and olivine map close up on olivine-bearing crater ejecta.

the olivine-bearing part of the unit correspond to etched, eroded terrains, whereas the olivine-poor parts appear to be less eroded and/or covered by fine material. The whole ridged plain unit could be olivine-enriched with respect to the Noachian surrounding terrains but olivine signature is likely masked in some parts by the presence of this fine material. The hypothesis that the whole unit could contain olivine is further supported by the detection of olivine-bearing ejecta of small craters in the olivine-poor regions, indicating the presence of olivine in the upper layers of the impacted crust (Figure 10f). Many ridged plains and flat intercrater units throughout the southern highlands show the same spectral and morphological characteristics and thus are likely olivine-bearing. In any case, this example, as the third one (Figure 9), emphasizes the complexity and the diversity of the relationships with thermophysical properties. That also explains why there is not a higher systematic trend of olivine with respect to thermal inertia in average (Figure 5).

[41] Olivine-bearing smooth crater floors are commonly found in close proximity to olivine-bearing flat plains as visible in the Figures 7–9. These craters are found throughout the southern highlands with diameters ranging from 10 km to more than 400 km (red-filled circles on Figure 6a). They commonly lack a central peak and exhibit a flat floor partially or entirely composed of olivine-bearing material. These craters are primarily found in Noachian units but their floors appear to be less heavily cratered than the surrounding terrains suggesting a younger age. They are mainly characterized by a high nighttime temperature and a low daytime temperature compared to surrounding terrains resulting from a higher thermal inertia. Some of these olivine-bearing smooth crater floors were previously detected across the southern highlands using TES, THEMIS, or CRISM [*Koeppen and Hamilton*, 2008; *Rogers and Fergason*, 2011; *Goudge et al.*, 2011].

[42] Figure 11 illustrates typical floor morphology for olivine-bearing bedrock. High nighttime and low daytime temperatures are observed; its floor has a rough and consolidated texture similar to those of flat plains, and no dune is observed at CTX scale where the olivine detection is strongest. Black and white arrows point out respectively the presence of wrinkle ridges at the center, and the lobate margin at the periphery of the crater. A three-dimensional view of this crater (Figure 11C) shows that this crater has a shallow floor relative to its diameter, so that a significant amount of material filled the crater. These characteristics are commonly observed throughout the highlands, and may indicate a widespread process that has occurred in the Martian history to form these deposits.

[43] Most craters (>80%) however have only a fraction of their floor spectrally dominated by olivine signature. In Figure 12 for example, the olivine signature is correlated to the western crescent shape on the crater floor, where higher nighttime and lower daytime temperatures are observed (Figures 12B and 12C). This part of the crater is more eroded and has a rough and pitted texture (Figures 12D and 12E), whereas the olivine-poor part corresponds to a dark surface of slightly higher elevation. This dark surface has a smoother texture than the olivine-bearing surface. In spite of
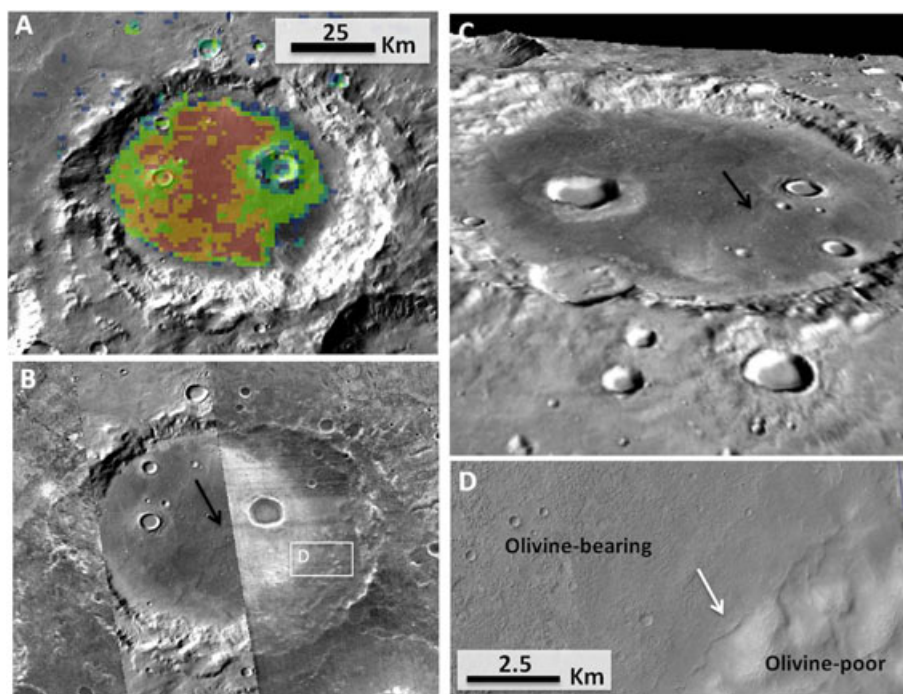
Figure 11. Example of an olivine-bearing crater floor in the southern highlands [–71.6°E, 36°S]. (A) Olivine map (OSP2 from 0.995 to 1.04) over THEMIS IR daytime mosaic; (B) Mosaic of THEMIS IR daytime (left part) and THEMIS IR nighttime (right part); (C) 3-D view of the area with a vertical exaggeration of 5. The black arrow indicates the presence of wrinkle ridge; (D) CTX detail showing the transition between olivine-bearing terrain and olivine-poor one (CTX_ID B02_010449_1443_XN_35S071W). A lobate margin is visible at the periphery of the deposit (white arrows).
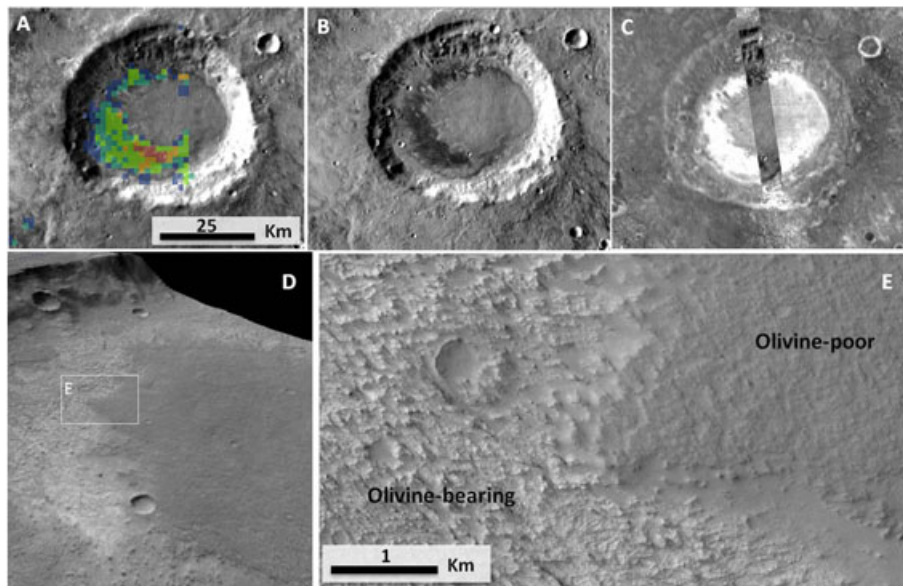
Figure 12. Example of a Martian high thermal inertia crater floor with olivine signature [41°E, 21.3°S]. (A) Olivine map (OSP2 from 0.97 to 0.995) over THEMIS IR daytime mosaic; (B) THEMIS IR daytime mosaic; (C) THEMIS IR nighttime mosaic; (D) 3-D view of the western part of the crater with vertical exaggeration of 15; (E) CTX image showing the transition between olivine-bearing and olivine-poor terrains (CTX_ID B07_012370_1589_XN_21S319W).

its lower thermal inertia possibly due to the presence of unconsolidated and/or finer-grained material, this surface could constitute a resistant capping unit deposited over the entire floor, and only been partly removed, exposing the underlying olivine-bearing deposits as previously proposed by *Rogers et al.*, [2009].

[44] Some crater floors display dunes or sand sheets spectrally dominated by olivine signature as illustrated in Figure 13. These deposits are relatively dark in comparison to other olivine deposits. Of special interest is the presence of olivine on rough and brighter bedrock on the opposite side of the dunes, which could be the source of this dark sand (Figure 13D). A systematic study of dark mobile sediments inside crater floors on Mars has revealed that they have not primarily been blown into the craters, but they more likely originate from inside the craters themselves [*Tirsch et al.*, 2009]. Although no clear relationship between the two olivine deposits inside this specific crater can be definitely proved, we consider that the olivine-bearing sand dunes observed in this crater as well as in other crater floors throughout the southern highlands could be of local origin as the result of erosion of the crater floor bedrock.

4.1.2. Ages of the Deposits

[45] In order to retrieve the crater age distribution, we have processed image sets providing large or full coverage of the investigated units with an easily pictured topography. For the largest surfaces, the daytime THEMIS temperature mosaic was used. This data set has an image resolution of ~100 m/pixel and provides very good topographic contrast because the slopes facing the Sun have a higher temperature than the opposite slopes. For smaller surfaces, we used CTX and HRSC higher-resolution images, enabling accurate measure of smaller craters.

[46] To estimate cratering retention ages from the measured crater size-frequency distributions on the chosen areas,

we have used the "*craterstats2*" software developed and described by *Michael and Neukum* [2010]. Ages have been derived by fitting a crater production function from *Ivanov* [2001] and by using the chronology function from *Hartmann and Neukum* [2001] to translate relative crater frequencies into absolute model ages; all ages given in this section are estimated with respect to this model. In cases for which we have observed at smaller crater diameters a deviation of the observed crater size-frequency distribution from the expected isochron, we also tested resurfacing scenarios. This evaluation has been performed with "*craterstats2*" as well. Because we are interested in the age of formation of the crater floor and intercrater plain units provided by the oldest crater retention age, we commonly did not consider small craters on the investigated units (diameter < 800 m with THEMIS data, < 500 m or lower with HRSC and CTX data). Examples of the crater measurements are given in Figure 14. Possible resurfacing events are plotted with triangles in the cumulative plots. The derived ages fall remarkably in the narrow 3.6 and 3.8 Ga range (Figure 15). This is in agreement with the early Hesperian age of the units (Hplm, Hpl3, and Hr) where plains are mainly found, but indicates possible formation during the Late Noachian for some of these plains and crater floors. Model ages seem to indicate the same age interval for both crater floors and flat plains within the uncertainties of the dating. As well, ages do not seem to depend on the longitude. Therefore, these deposits were likely emplaced at the same time.

4.1.3. Composition

[47] As seen on the olivine global map, olivine deposits of the southern highlands have both Type 1 and Type 2 compositions. Type 1 composition is found in extensive deposits that have been identified as Hesperian-aged plains and crater floors. The smaller localized exposures of Type 2 olivine
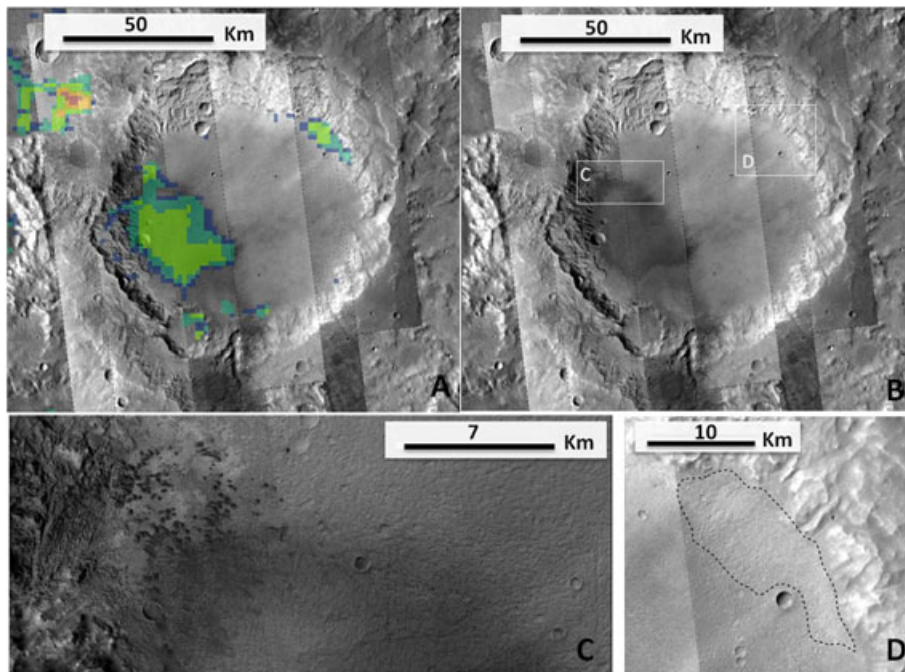
Figure 13. Example of olivine-bearing sands and dunes on a crater floor located in Terra Tyrrhena [67.7°E, 2.9°S]. (A) Olivine map (OSP2 0.98 to 1.04) compared to a CTX mosaic (B) with daytime THEMIS IR mosaic in the background (CTX_ID from left to right P03_002282_1769_XN_03S293W, P07_003627_1766_XN_03S292W, P20_008901_1754_XN_04S292W, P14_006607_1783_XN_01S292W, B18_016549_1761_XN_03S291W, B03_010747_1776_XN_02S291W). (C, D) Two close-ups of the crater floor are shown with CTX images.

composition correspond to areas of these extended deposits where the olivine signature is stronger. These signature variations could be attributed to variations in composition and/or abundance and/or grain size. We mainly attribute these variations to an abundance effect resulting from the heterogeneous cover by pyroxene-bearing mobile material. In these deposits, a pyroxene signature is always visible and the strength of its 2 μm band is commonly anticorrelated with the olivine signature. This is due to the fact that the addition of pyroxene material decreases the olivine signature. Such a spectral evolution is seen in the extensive volcanic plains presented in Figure 10. The visual inspection of spectra extracted from olivine-poor to olivine-enriched terrains confirms that the variations of OSP2 parameter and olivine spectral features result from the variable abundance of low albedo pyroxene-bearing material (Figure 16). The spectral ratio technique then reveals an olivine signature in regions where the value of olivine parameter is small.

4.1.4. Origin and Implications

[48] The olivine-bearing Hesperian flat plains and crater floors usually exhibit distinct higher thermal inertia than the surrounding terrains. These thermal properties are consistent with their rough and pitted morphology retrieved from CTX and HiRISE images, corresponding to eroded bedrocks. Both the olivine-bearing Hesperian plains and the olivine-bearing crater floors result from infillings. A sedimentary origin could thus be proposed. However, the fact that the surrounding terrains have a distinct composition and the lack of sources for olivine-bearing materials strongly opposes such a sedimentary origin. Instead, the characteristics of these deposits support a magmatic origin. Emplacement mechanisms considered for the olivine-bearing units could be volcanic flows or igneous intrusions. Existing observations favor the first scenario. Specifically, olivine-bearing lava flows resulting from fissure eruptions (possibly through impact-related fractures) might have buried crater floors and intercrater depressions. The volcanic extrusive origin is also consistent with the presence of wrinkle ridges in both plains and crater floors, as well as lobate margin at the periphery of crater floor deposits. Such structures were observed on the lunar surface and were interpreted as the result of fissural volcanism [*Leverington*, 2004]. Volcanic infilling was also proposed by *Rogers and Fergason* [2011] to explain the olivine-bearing deposits in intercrater plains and in crater floors of the region of Tyrrhena Terra. Our additional observations show that this mechanism operated at a global scale and could explain numerous olivine deposits of the southern highlands. The magma could have reached the surface through fractures and cracks in the basement rock likely caused by previous impact events, possibly related to the formation of the large basins during the late heavy bombardment [*Gomes et al.*, 2005].

[49] The dating retention ages of these surfaces revealed that the last event that produced these deposits preferentially occurred during the early Hesperian between 3.8 and 3.6 Ga (Figure 15). This suggests a period of global olivine-enriched volcanism, which filled craters and intercrater plains through fractures throughout the Martian surface during the late Noachian/early Hesperian. Material derived directly from the Martian mantle is expected to be significantly more mafic than the surrounding rocks. The olivine enrichment of the deposits reported here is thus well consistent with
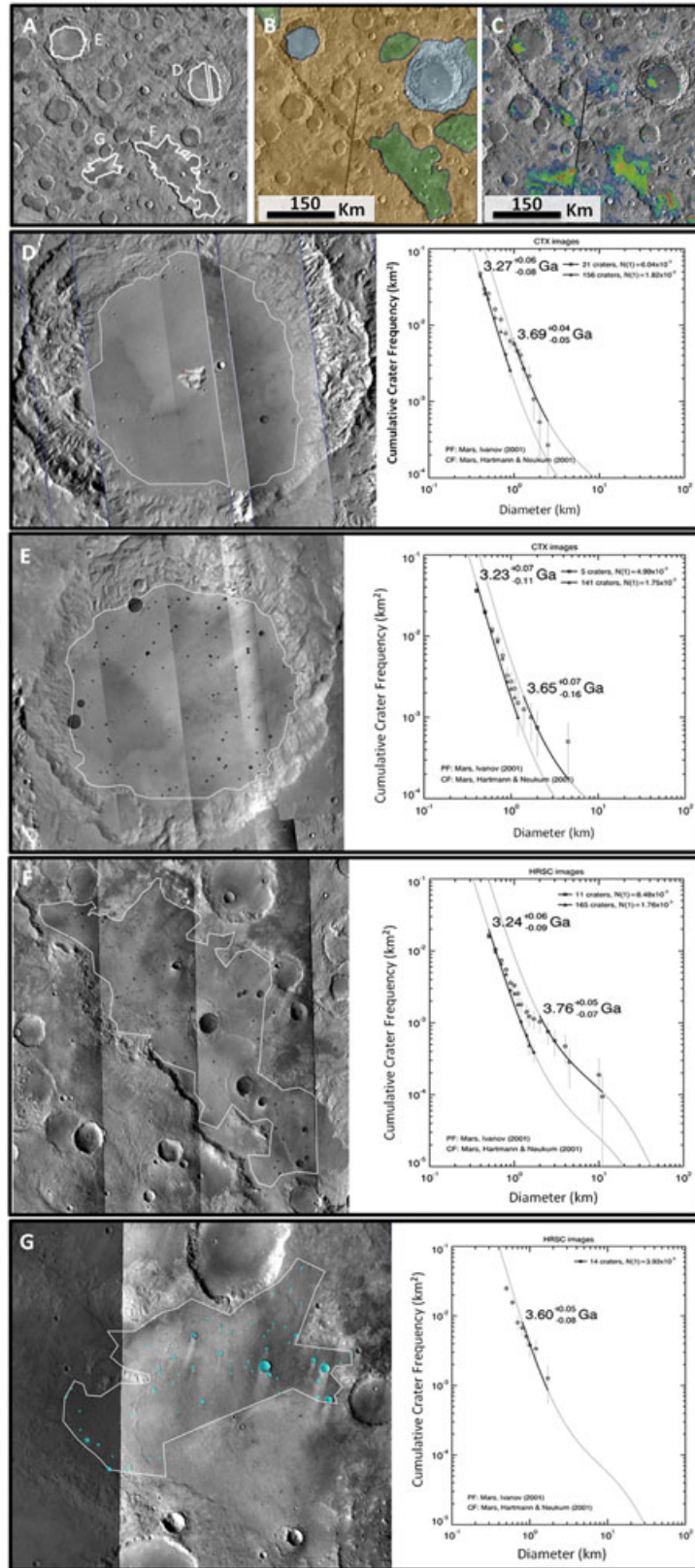
Figure 14. Contextual images of dated flat plains and smooth crater floors: (A) THEMIS IR daytime mosaic, white line surrounds dated flat plains and smooth crater floors. (B) USGS geological map (brown: Noachian units; green: Hesperian units; grey: impact crater material) [*Skinner et al.*, 2006]. (C) olivine map over THEMIS IR daytime mosaic. left: CTX (D, E) and HRSC (F, G) close-up on flat plains or smooth crater floors; right: corresponding crater-size frequency distribution, observed crater measurements are plotted with squares, possible resurfacing events are plotted with triangles, derived age is indicated.
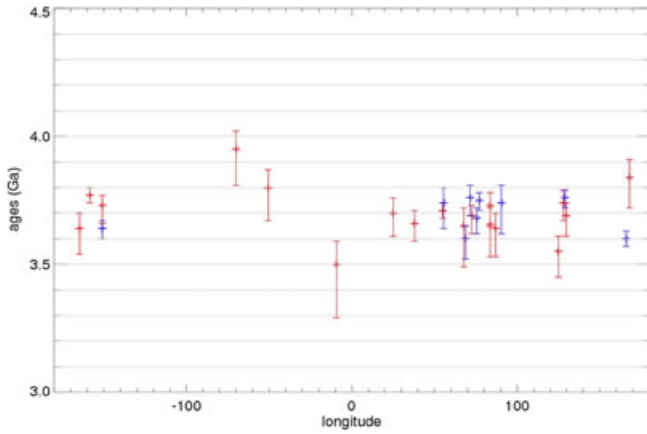
Figure 15. Age of investigated olivine-bearing deposits as a function of longitude: red crosses correspond to crater floors, and blue crosses to flat plains.

a mantle magma origin. This global Martian volcanic event could be similar to the lunar mare formation that occurred mainly between 3.3 and 3.7 Ga, as the result of the radiogenic heating of the lunar mantle [*Schultz and Spudis*, 1983; *Hiesinger et al.*, 2003; *Wieczorek and Phillips*, 2000].

[50] Such a large planet-wide volcanic event can be questioned. Widespread volcanic flooding has been invoked for the formation of Hesperian ridged plains that resurfaced the northern lowlands [*Head et al.*, 2002]. This resurfacing was actually considered to be global in nature and also responsible for the formation of Hesperian-aged volcanic plains exposed in the southern highlands [*Head et al.*, 2002]. Our results further emphasize the importance of events occurring during the Early Hesperian, with significant volcanic activity, corresponding perhaps to a peak global flux [*Greeley and Schneid*, 1991; *Tanaka et al.*, 1992]. Such planetary-scale activity could also account for the olivine

deposits in the northern plains and Valles Marineris (see sections 4.3.2 and 4.4.2).

[51] The olivine-bearing settings discussed in this section are compositionally distinct from the olivine-poor degraded and older high-standing terrains. Such a trend was already reported regionally in Terra Tyrrhena [*Rogers and Fergason*, 2011], and our investigation demonstrates that this trend is common in the entire southern highlands. It is not clear if these differences are due to true lithologic differences, and/or to differences in alteration/resurfacing between them. It may be possible that the deficiency in olivine in most Noachian soils (relative to Hesperian bedrock) comes from the derivation from older, olivine-poor bedrock. However, there are several observations showing that some crustal Noachian rocks are also enriched in olivine (see section 4.5) [*Skok et al.*, 2012; *Loizeau et al.*, 2012]. From the correlation of olivine-enriched terrains and their high thermal properties, *Bandfield et al.* [2011] alternatively assumes that the low content of olivine in the ancient soils could result from olivine dissolution by aqueous alteration. However, the correlation with high thermal inertia is not clear, as we observe olivine associated with a wide range of thermal inertia. Moreover, the presence of olivine-bearing material derived from local sources in the early Hesperian questions the quasi-absence of similar olivine-bearing material in the older highlands. Hundreds of impact craters and crater ejecta that have excavated the Noachian highlands have been observed with OMEGA and CRISM: the excavated rock has much less suffered from a potential surface alteration, and sample deeper layers, but olivine-bearing craters are not dominant. This would indicate that the Noachian crust was either poorer in olivine than the younger Hesperian plains and crater floors; alternatively, the Noachian crust could have been altered at depth so as to decrease its olivine content.
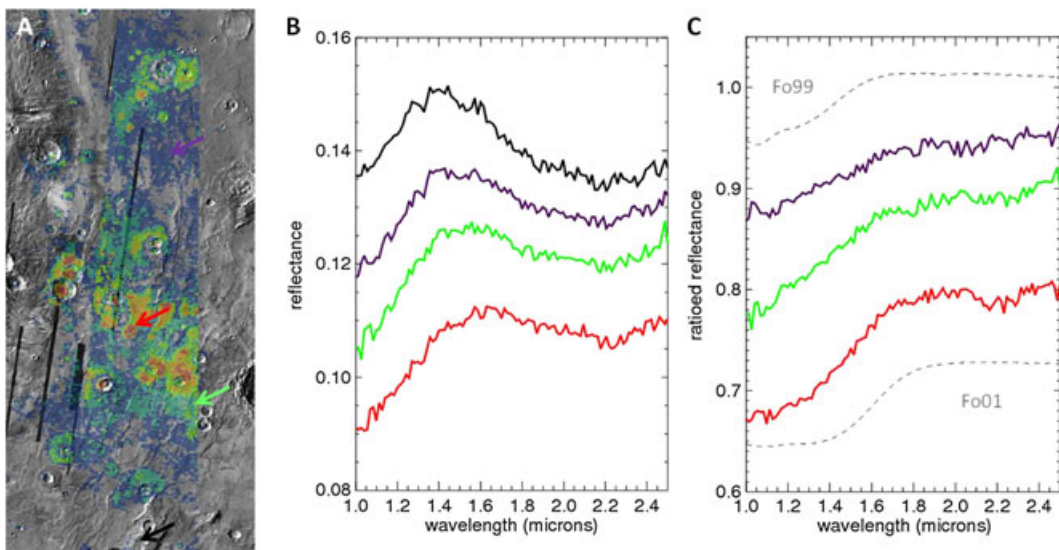

Figure 16. (A) Olivine map (OSP2 parameter from 0.99 to 1.04) over ridged plains located south of Valles Marineris (same as those illustrated in Figure 10). (B) Spectra extracted from location pointed by color arrows in (A). The corresponding ratioed spectra shown in (C) were obtained by dividing them by the black spectrum extracted from olivine-poor unit. They are compared to two RELAB library olivine spectra.

4.2. Olivine Deposits on the Terraces of Main Basins

4.2.1. Settings

[52] Olivine is found in many deposits around the three main basins: Isidis, Argyre, and Hellas. Olivine around the Isidis basin is found in rather unique settings and was extensively described and discussed in previous works [*Hoefen et al.*, 2003; *Hamilton and Christensen*, 2005; *Mustard et al.*, 2007, 2009; *Tornabene et al.*, 2008; *Poulet et al.*, 2009b; *Bishop et al.*, 2012]. Olivine is detected on a 30,000 km^2 olivine-enriched area in the region of Nili Fossae, which displays exposures of bedrock outcrops exhibiting the
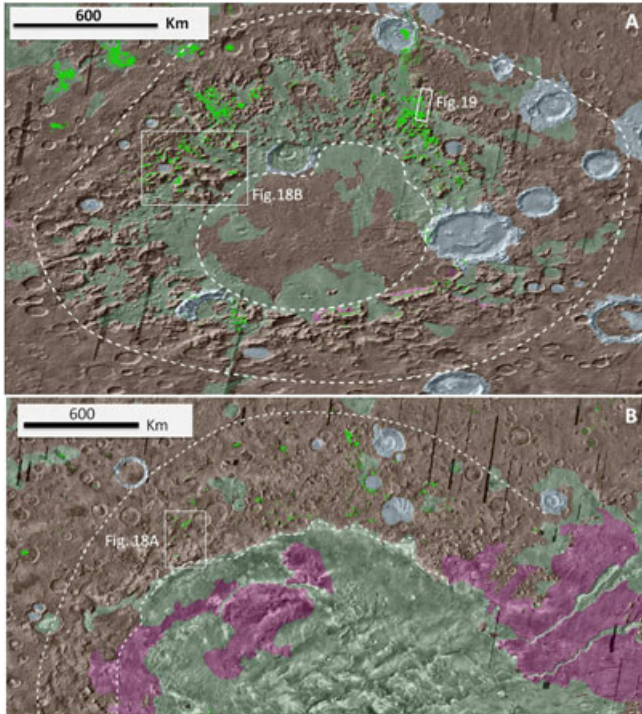

Figure 17. USGS Units map of Argyre (A) and north/west part of Hellas (B) regions (brown: Noachian; green: Hesperian, pink: Amazonian, grey: large impact structures) [*Skinner et al.*, 2006] with olivine detection in light green. The dashed lines roughly define the layouts of the terraces of the basin.

largest exposures of olivine-dominated rock units on Mars. Olivine is also detected in a high thermal inertia unit in the southwestern portion of the Isidis basin at the boundary between the Lybia Montes unit and the inner basin.

[53] The olivine-bearing deposits around Argyre and Hellas are different from Isidis ones (Figures 17). The detections are primarily distributed along the northern part of both terraces with only few olivine signatures detected in the southern rim of Argyre. This dichotomy between the northern and the southern rims can result from the presence of seasonal ices and dust at high latitudes as well as resurfacing processes, which could mask the olivine signature. Distribution of these deposits around the Argyre basin clearly takes the form of discontinuous exposures located on isolated hills of Noachian age (Npl1 unit) (Figure 18B). Several of these hills have a relatively warm nighttime temperature indicative of high thermal inertia that can reach 550 tiu [*Bandfield and Rogers*, 2008]. These values are consistent with rocky surface or limited exposures of bedrock. Figure 18C shows that the highest olivine detections are well correlated with the warmest nighttime temperature parts of the hills, thus corresponding to the most eroded and exposed surface. In contrast, olivine-poor surfaces have a low nighttime temperature and appear covered by a sand layer that could hide the olivine signature. These olivine-bearing hills are surrounded by Hesperian plains (Hpl3 unit), which also exhibit olivine signatures in some areas. These plains could be related to Hesperian olivine-bearing flat plains observed throughout the southern highlands and described in the previous section. However, we cannot totally exclude that these olivine signatures could originate from material eroded from the olivine-enriched hills and transported over Hesperian plains [*Bandfield et al.*, 2011]. The olivine deposit distribution around the Hellas basin is not as clear as for Argyre because of intense resurfacing processes that strongly affected this region. Olivine detections are found in fewer occurrences with weaker signatures, but still in the same Noachian hilly structure (Nh1 unit) as for Argyre (Figure 18A).

[54] Some olivine detections on the terraces of the two main basins were reported by previous studies using TES and THEMIS IR data [*Koeppen and Hamilton*, 2008; *Bandfield and Rogers*, 2008; *Lane and Goodrich*, 2010]. Figure 19 compares THEMIS IR olivine detections mapped in purple
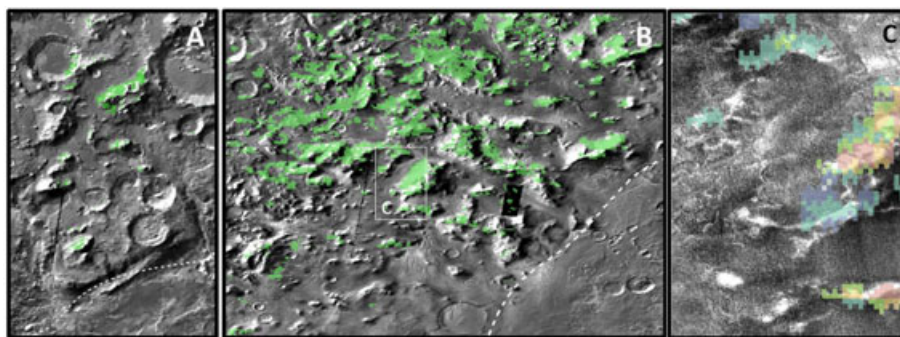
Figure 18. (A) Close-up of the Hellas basin terrace with olivine detection in green superimposed on a THEMIS IR daytime mosaic. (B) Close-up on the west of Argyre basin terrace with olivine detection in green superimposed on a THEMIS IR daytime mosaic. (C) Close-up on the area indicated with a white square in Figure 18B, with olivine detections from blue to red, superimposed on a THEMIS IR nighttime mosaic.

[Lane and Goodrich, 2010] and OMEGA olivine detections mapped in green for a region of the northeast of the Argyre rim (marked by a white square in Figure 17A). The detections
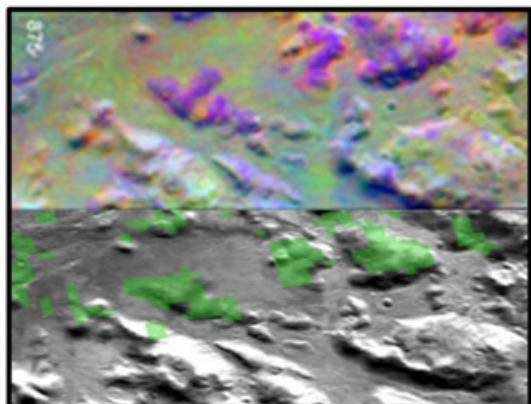

Figure 19. Comparison between THEMIS and OMEGA observations. (top) THEMIS DCS scene I08016003, olivine appears as purple [Lane and Goodrich, 2010]. (bottom) OMEGA observation of the same region with OMEGA-based olivine detection in green superimposed on a THEMIS IR daytime mosaic.

are remarkably consistent and show olivine-bearing hills surrounded by an olivine-poor smooth and flat surface.

4.2.2. Composition

[55] Based on the spectral parameter approach, the circum-Argyre and Hellas olivine is preferentially of Type 2 with intermediate spectral features that can correspond to either Mg-rich olivine with large grain size, Fe-rich olivine with small grain size or an intermediate composition. To assess quantitatively the composition, the radiative transfer model, described in section 2.2, was applied on 12 spectra extracted from these regions whose four examples are shown in Figure 20. Although based on a limited number of spectra, this study can give some preliminary trends about the composition of these deposits. The derived olivine abundances range from 12 to 27 vol % mixed with about 30% of pyroxenes and 40% of plagioclase. Best fits are mainly obtained using the third mixture (both forsterite and fayalite end-member with a fixed grain size at 100 μm; see section 2.2) with forsterite abundance larger than the fayalite one, and with the first mixture (forsterite end-member only) but with grain size mainly >100 μm. With NIR data, it is tricky to derive the exact composition in Mg content, but both spectral features and modeling are in favor of an intermediate to slightly forsteritic composition as found by TES [Koeppen and Hamilton, 2008; Lane and Goodrich, 2010].
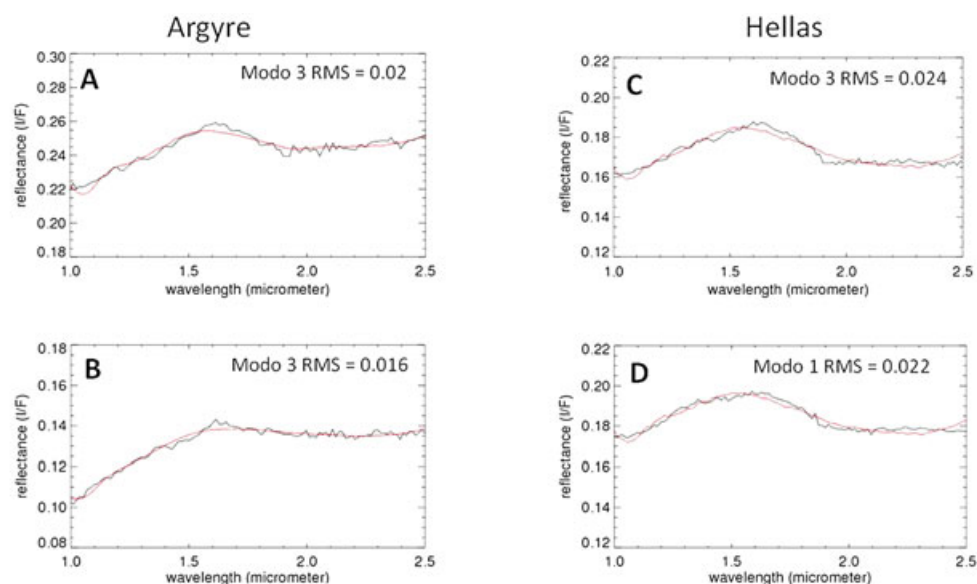
		A		B		C		D	
		Abundance	/grain size	Abundance	/grain size	Abundance	/grain size	Abundance	/grain size
olivine	Forsterite	17	100 μm	16	100 μm	12	100 μm	13	83.7μm
	Fayalite	6	100 μm	1.6	100μm	0	0	0	0
Pyroxene	LCP	13		15		7		9	
	HCP	15		10		21		19	
Plagioclase		39		58		55		52	
Dust		9		0		4		6	

Figure 20. Example of spectra extracted from the Argyre and Hellas basins terrace and compared to their best fit model in red. Each spectrum corresponds to one OMEGA pixel. Table gives modeled abundance of olivine, pyroxene, plagioclase, and dust. RMS (residual mean square) and starting conditions are indicated (Modo 1: forsterite end-member alone with its grain size as a free parameter; Modo 3: both fayalite and forsterite end-member with grain size fixed at 100 μm)

4.2.3. Origin and Implications

[56] The unique settings and composition of olivine deposits in the region of Nili Fossae and in the southwestern rim of the Isidis basin compared to the two other major basins could indicate different origins. Three hypotheses have been discussed to explain the Nili Fossae olivine deposit emplacement relative to the formation of the Isidis basin: preimpact igneous intrusives [*Hoefen et al.*, 2003] or extrusive olivine-enriched layered basalts [*Hamilton and Christensen*, 2005], contemporaneous Isidis-related impact melt [*Mustard et al.*, 2007], or postimpact volcanism [*Tornabene et al.*, 2008]. Because the numerous observations of olivine-bearing extended plains and crater floors explained by volcanism infilling throughout the southern highlands make the third process pretty common on the Martian surface and the principle source of olivine-bearing areas on the southern highlands, we consider that a postimpact formation by erupted lava flows originated from Isidis impact related fractures could be a realistic formation process for southwestern rim deposits at least. However, the very large grain sizes (several millimeters) and the high abundance (40%) of Nili Fossae deposit are unique on Mars and significantly differ from the composition of the early Hesperian deposits. As already discussed in *Poulet et al.* [2009b], such olivine megacrysts could be in favor of intrusive rocks rather than extrusive rocks.

[57] Olivine distribution around the two main basins Argyre and Hellas clearly takes the form of discontinuous olivine-bearing mixtures exclusively localized on hills associated with Noachian units Nplh and Nh1 that are among the oldest geologic units on Mars. These unique distribution and age strongly suggest that their formation is related to the basin formation event. Numerical simulations of basin formation indicate that lower crust/upper mantle material could be emplaced as discontinuous patches on the terrace zone of the final impact basin. These investigations were first applied to understand the mechanism of formation of lunar basins but they can be extrapolated to Mars for basin as large as Argyre or Hellas [*Stewart*, 2011]. This would favor the origin of olivine-bearing hills observed on the terrace of Argyre and Hellas basins as olivine-bearing material excavated from the upper mantle/lower crust during the impact. The enrichment in olivine may reflect the composition of the upper mantle/lower crust proposed to be olivine-rich [*Elkins-Tanton et al.*, 2003, 2005].

[58] The early stages of planetary differentiation were driven by the release of accretion energy, with large masses of molted rock constituting a "magma ocean". However, the depth of this magma ocean and the fate of its further crystallization, depending on the planetary size and collision history, in particular with respect to possible giant impacts, are still poorly constrained, except possibly for the Moon [*Warren*, 1985, *Nemchin et al.*, 2009]. For Mars, modeling shows that this magma ocean could have crystallized from the base up, leading to an unstable stratification, with dense iron-rich material on top and less dense Mg-rich material below, then later overturning to a stable configuration. The upper mantle would be composed of ~60% olivine with a Fo number smaller than 25 before, and with a large Fo number after overturn [*Elkins-Tanton et al.*, 2005; *Debaille and Brandon*, 2011]. Our results, interpreted as mantle ejecta from the Argyre and Hellas impacts, with a composition closer to forsterite than to fayalite, support mantle overturn. A similar conclusion was suggested by *Koeppen and Hamilton* [2008].

4.3. Olivine Deposits in the Northern Plains

4.3.1. Settings

[59] In the northern plains, variable atmospheric conditions combined with the presence of dust and seasonal icy clouds and frosts partly mask the signature of surface materials and make harder their detection, identification and mapping than in the low albedo southern highlands. Previous observations have shown that many low albedo regions of the northern plains are dominated by a blue slope in the near infrared [*Poulet et al.*, 2007]. A careful visual inspection reveals that this lower blue slope can be associated with a slightly deeper 1 μm spectral feature in some areas due to olivine spectral signature. These detections are primarily made thanks to OSP3, which is much less sensitive to the overall bluish slope of the spectrum. They are distributed in three main geological contexts within the entire northern plains, and noticeably in Chryse and Acidalia Planitia, and Utopia Planitia: ejecta of craters of various sizes; sand dunes accumulated in larges craters floors; and in extended and continuous deposits (Figure 21).

[60] Figure 22 is centered on the region of Chryse Planitia. This region is one of the less dusty regions of the northern lowlands, which allow assessing its mineralogy. Olivine signatures are associated with ejecta of some relatively small craters [5–20 km]. These olivine-bearing crater ejecta exhibit
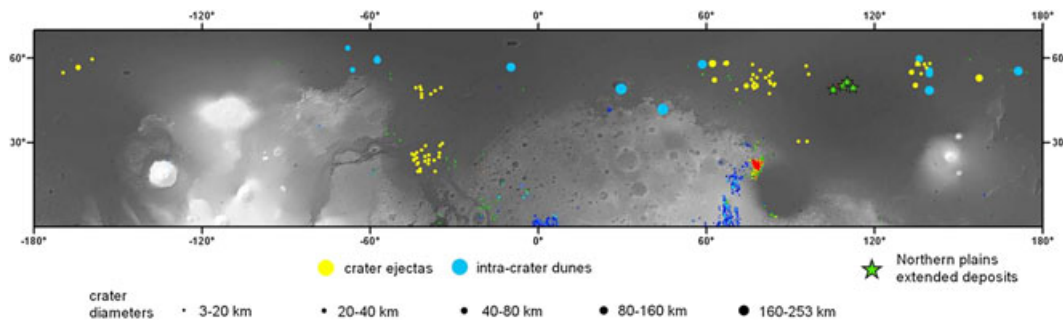

Figure 21. Northern plains olivine global map over MOLA map with locations of main geological settings: crater ejecta, intracrater dunes, or sandy deposits (circle symbol diameters are function of crater diameters), and large olivine-enrich deposits in Utopia Planitia.
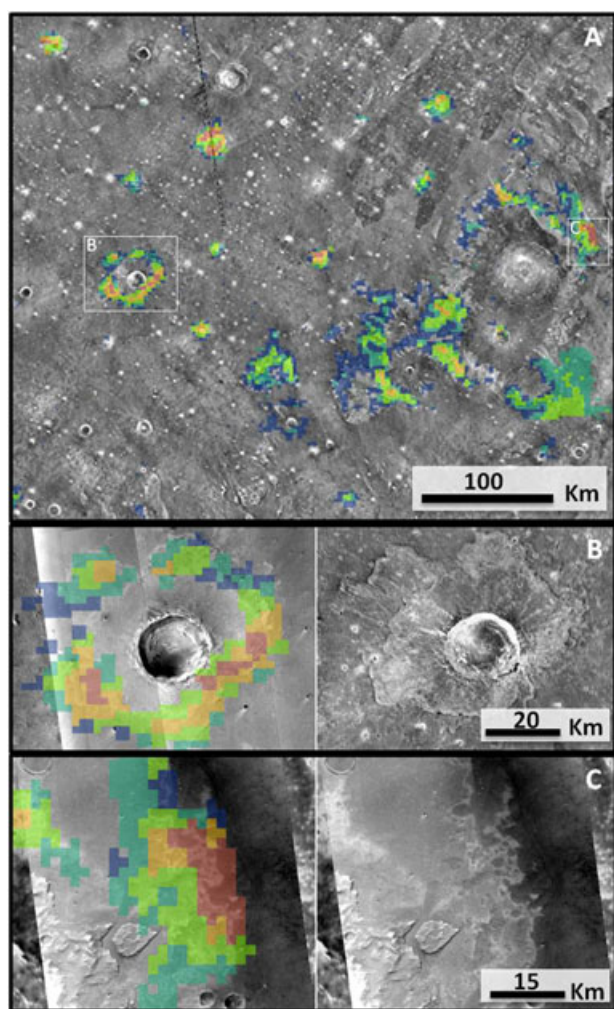
Figure 22. (A) Olivine map (OSP2 from 0.97 to 1.0) in Chyse Planitia [–37.5°E, 23.9°N] overlying THEMIS IR nighttime mosaic, with two close-ups (B) olivine detection (OSP2 from 0.975 to 1.0) on CTX images (left) (CTX_ID P04_002655_2033_XI_23N040W, P17_007481_2053_XN_25N040W, B05_011542_2024_XN_22N 039W) and corresponding THEMIS IR nighttime mosaic (right) and (C) olivine detection (OSP2 from 0.972 to 0.99) on CTX image (left) and CTX image only (right) (CTX_ID P14_006571_2047_XN_24N032W).

high nighttime and low daytime temperatures indicative of a more rocky and/or a less dusty surface than the olivine-poor surrounding terrains. Conversely, crater ejecta that do not show any olivine signature have lower nighttime and higher daytime temperatures similar to the plains. This likely results from a dust cover that hides surface material and then could explain the lack of olivine signatures. Given the relatively small size of craters that excavated olivine, the olivine-bearing material is present near the surface. Figure 22B shows an enhancement of the olivine signature in a double ejecta crater (crater diameter ∼ 20 km, middle left white square of Figure 22A), but olivine is mainly correlated to the distal lobate ejecta. This unique setting probes the vertical stratigraphy of the region; a near-surface olivine-bearing layer overlies olivine-poor material, as revealed by the absence of signature in the proximal lobate ejecta.
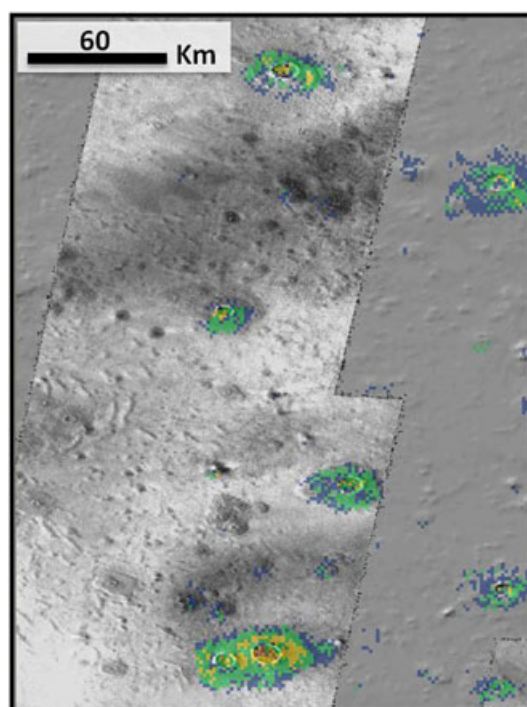

Figure 23. Olivine-bearing ejecta of small craters (<20 km) in Utopia Planitia, centered in [76°E, 52.6°N] (olivine detections (OSP2 from 0.935 to 0.96) are superimposed on THEMIS IR daytime mosaic).

[61] At the eastern proximity of this area, olivine is also associated with a rather large area centered at –34.6°E and 22°N (Figure 22C). *Edwards and Christensen* [2011] reported for the same surface a thermal inertia of ~820 tiu consistent with exposed in-place rock. This unit could represent olivine-bearing outcrops of a more extended region possibly connected to the western olivine-bearing crater ejecta region.

[62] Some olivine weak signatures close to the detection threshold are also detected in lobate ejecta of smaller sized craters (<20 km) in the low albedo region of the N-W of Utopia Planitia and Acidalia Planitia (Figures 21 and 23). These signatures indicate that the shallow subsurface of this region is also primarily basaltic in nature as the lowland regions discussed above.

[63] As already reported by *Bibring et al.* [2005], olivine-bearing ejecta are found around craters with large diameters (>20 km) at high latitudes (Figure 24). The HiRISE image (Figure 24B) of one olivine-bearing area shows typical elongated patterns usually visible for fluidized ejecta lobes. This material was excavated from beneath the northern plains cover, exhuming the underlying crust. At these high latitudes, olivine is also found associated with dark sands accumulated in craters with diameters ranging from 20 to 300 km (Figure 25).

[64] Of special interest is the olivine detection, not associated with craters as commonly observed in the northern plains, but to a 500 km long unit located in the low albedo part of the Utopia Planitia region [111.2°E, 49.6°N] (Figure 26). The olivine-bearing deposit is thermophysically distinct from the surrounding dusty terrains: it has a low albedo and exhibits rough and pitted texture typical of
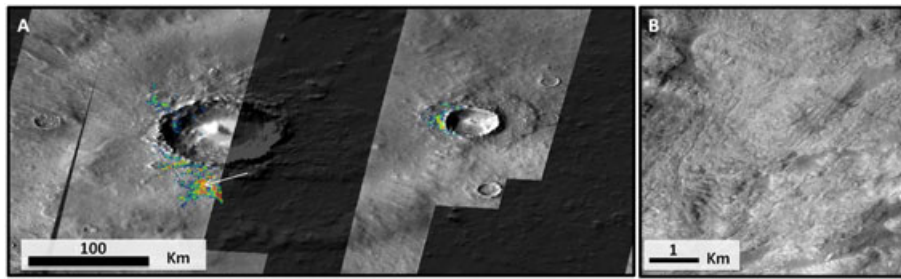
Figure 24. (A) Olivine in two large crater ejecta [60.5°E, 58°N] (olivine detections (OSP2 from 0.995 to 1.04 for left crater and from 0.96 to 0.99 for right crater) are superimposed on THEMIS IR daytime mosaic). (B) HiRISE close-up showing fluidized ejecta indicated by the white arrow (HiRISE_ID PSP_002071_2375).
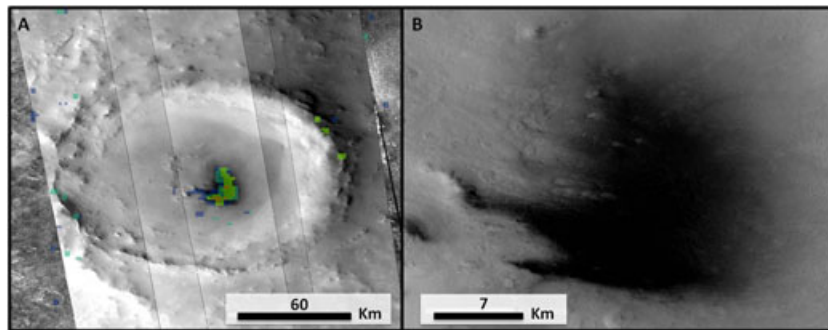
Figure 25. Olivine-bearing sand sheet in a crater located at [139.7°E, 48°N] (OSP2 from 0.975 to 1.02) (CTX images on background, CTX_ID from left to right B05_011542_2024_XN_22N039W, P18_007883_2284_XN_48N220W, B03_010665_2284_XI_48N220W, P17_007527_2284_XN_48N220W, P16_007382_2284_XN_48N219W) (A) with CTX close-up (B).

eroded lavas (Figure 26D). It is located at the boundary between the Elysium formation unit (Ael3) and the Vastitas Borealis formation unit (Hvm, Hvg), respectively defined as Amazonian and Hesperian in age [*Skinner et al.*, 2006].

[65] The signature of the olivine deposits in these regions is significantly modified by the surface dust coverage and large atmospheric opacity, which complicates its spectral analysis and the application of the radiative transfer model to derive the modal mineralogy. Overall, the ratioed spectra have a rather strong and spectrally extended signature, more consistent with Type 2 olivine.

### 4.3.2. Origins and Implications

[66] The northern plains of Mars cover a Noachian basement, and have experienced widespread volcanism, sedimentary deposition, secondary geologic processes, and effects due to climate changes during the Hesperian and Amazonian. Detections of olivine in ejecta of relatively small craters in the region of Chryse Planitia could come from an underlying olivine-bearing layer on this region, some hundreds of meters deep at maximum given the size of the craters (5–20 km of diameter). The presence of this layer is also supported by the large olivine-bearing outcrops found ~100 km east of these ejecta, which could constitute exposed and eroded parts of this layer. These observations are in agreement with *Salvatore et al.* [2010] observations made with CRISM, of olivine signatures in crater ejecta and in bedrock exposures in crater rims, walls, and central peaks of the region of Chryse Planitia and Acidalia Planitia. They conclude that these detections primarily result from a basaltic unit just below the surface, which has been buried by sediments driven by diverse processes. Observations of olivine in small crater ejecta in the N-W part of Utopia Planitia indicates that the underlying olivine-bearing layer observed in the Chryse Planitia and Acidalia Planitia regions could extend much further in the northern plains consistent with a widespread volcanism episode during the Hesperian epoch [*Head et al.*, 2002]. As mentioned previously, this volcanism could be related to Hesperian olivine-bearing lava flows, which have also filled intercrater plains and crater floors throughout the southern highlands.

[67] Olivine-bearing dunes, accumulated on the floor of large craters in the northern plains of Vastitas Borealis, were already reported by previous works [*Rogers and Christensen*, 2003; *Bibring et al.*, 2005]. It cannot be entirely ruled out that these dunes are transported material originated from an olivine-bearing or basaltic region of the southern highlands. However, the large distances separating these craters floors from the closest highlands basaltic terrains make this scenario unlikely [*Greeley and Kraft*, 2001]. In addition, the lack of convincing evidence for distinct material that would also have been transported input into the craters, combined with many examples of dark sediment emerging out from craters [*Tirsch et al.*, 2009], support the fact that these dunes are predominantly

constituted by material excavated from olivine-bearing local sources. These craters are large enough to have excavated the underlying Noachian crust buried hundreds of meters
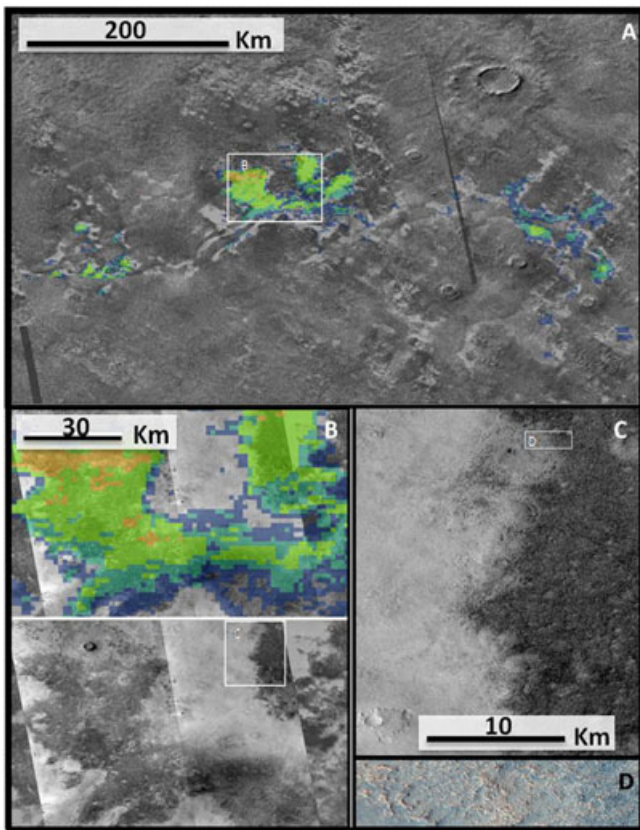
Figure 26. (A) Extended deposits in Utopia Planitia mapped as green stars in Figures 6a and 21, centered on [110.8°E, 49.3°E] (Olivine detections (OSP2 from 0.98 to 1.04) are superimposed on THEMIS IR nighttime mosaic). (B) Close-up of the region over CTX mosaic (CTX_ID from left to right P02_001911_2305_XI_50N251W, P22_009809_2305_XN_50N250W, THEMIS IR night mosaic in background). (C) CTX image covering the transition boundary between low albedo olivine-bearing terrains and olivine-poor dusty terrains. (D) HiRISE close-up of olivine-bearing unit (HiRISE_ID ESP_016534_2305).

to a km below the surface [*Head et al.*, 2002]. Such an excavation process was already proposed for some large craters [20–230 km] in the northern plains by *Carter et al.* [2010] who found olivine-bearing outcrops associated with phyllosilicates primarily located the central peaks, by using CRISM targeted images. In some craters, mobile olivine-bearing material is found in proximity of these central peaks, suggesting erosion and aeolian transport (Figure 25). Therefore, olivine dunes observed in these craters are interpreted to be material eroded from olivine-rich crustal material excavated by the impact. Olivine found in the ejecta of very large craters has very likely the same origin.

[68] The olivine-bearing deposit found in the Utopia Planitia region shows an exposed rough surface, similar to those found in olivine-bearing flat plains and crater floors of the southern highlands. This deposit could be an exposure of buried Utopia Planitia Hesperian plain, and thus another witness of the Hesperian widespread volcanic episode. However, its unusual emplacement in the Amazonian Elysium formation (Ael3) unit makes an origin associated with the Amazonian Elysium volcanism still possible, which would imply an olivine-enriched volcanic episode during a recent stage of Elysium activity. This deposit would be the only olivine-bearing deposit of this study detected in association with an Amazonian volcanic unit.

4.4. Olivine in Valles Marineris
4.4.1. Settings

[69] Numerous olivine-bearing deposits are found throughout Valles Marineris, with the strongest signatures in Aurorae Chaos and Eos, Ganges, and Hyrdatoes Chasmata (green stars on Figure 27A). Some of these deposits were previously reported by *Christensen et al.* [2003] and *Edwards et al.* [2008] in the region outlined as a white square in Figure 27A. They exhibit the strongest olivine signatures (mainly Type 2 olivine) and are mainly localized on the side of the canyon floor or associated with chaotic floor as defined by *Sharp* [1973].

[70] One of the largest deposits, previously detected by *Edwards et al.* [2008], was found close to the north wall of Aurorae Chaos (Figure 28). As with other deposits reported on the side of the canyon floor, it has a high albedo and a warm nighttime temperature. This thermal inertia, formerly reported to be larger than 600 tiu by *Edwards et al.* [2008], is consistent with the consolidated morphology
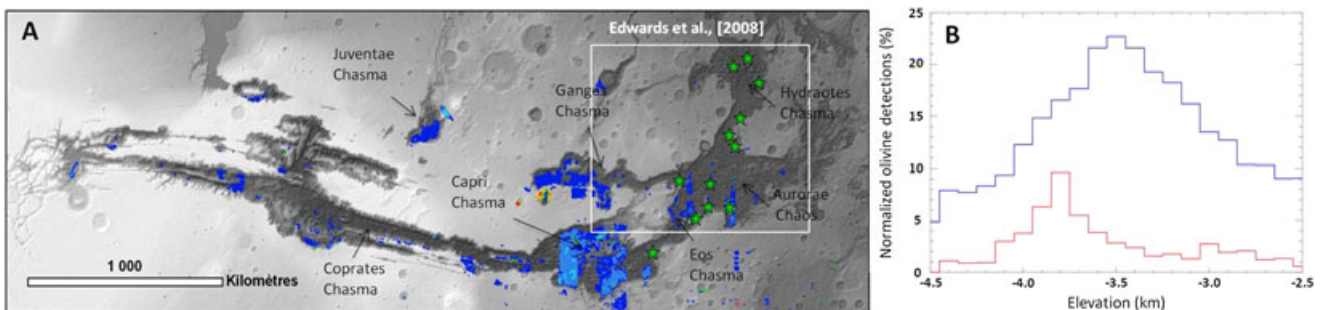
Figure 27. (A) Regional view of olivine global map over Valles Marineris. Green stars point to locations of olivine-bearing outcrops. White square indicates the region studied by *Edwards et al.* [2008]. (B) Normalized elevation histograms of Type 1 (blue line) and Type 2 (red line) olivine found in this region (histogram of type 2 olivine is multiplied by 10 for a better visualization).
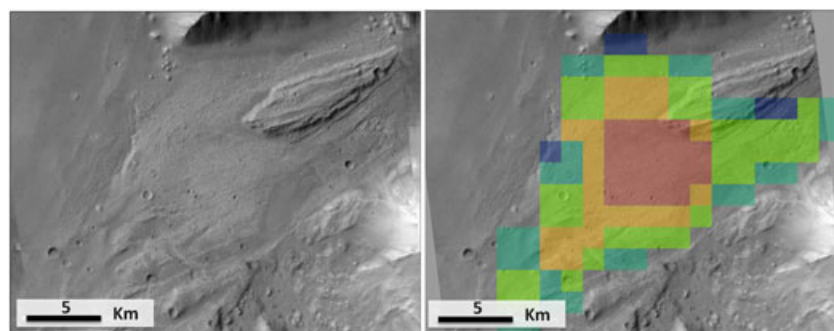
Figure 28. Example of olivine-bearing outcrop (OSP2 from 0.97 to 1.02) located at [–34.6°E, 3.2°S] with typical bench-forming morphology (CTX image, ID P20_008707_1757_XI_04S034W).

revealed by the CTX image (Figure 28). These observations strongly support a bedrock material exposed on the floor of Valles Marineris and surrounded by aeolian mobile materials.

[71] Figure 29 shows a close-up view of the olivine map in the south of Aurorae Chaos in chaotic terrains. Olivine is detected in sandy deposits that embay hills and small mesas but the strongest signatures are associated with outcrops with characteristics very similar to the previous example found in the north of Aurorae Chaos. Two examples are chosen to illustrate the bench-forming nature of the outcrops (Figures 29B and 29C). Both have the same elevation (respectively –3770 m and –3760 m in comparison to –3940 m for the floor) and are dominated by mounds that could represent the remnant of an overlying olivine-poor layer. Similar settings were found in Hydraotes Chasmas

where olivine is detected in outcrops present under chaotic mounds at an altitude of about –3900 m. These outcrops are exposed up to 500 m above the canyon floor.

[72] To search for a regional trend in outcrops elevation, we binned olivine detection found in Valles Marineris as a function of MOLA elevation (Figure 27B). This histogram shows that Type 2 olivine detections (red histogram), which corresponds to the olivine-bearing outcrops, are mainly found between –3600 and –3900 m. As previously observed by *Edwards et al.* [2008], this unique distribution in elevation indicates that these outcrops are representative of a large contiguous and thin layer throughout a large region of the Valles Marineris canyon system.

[73] Other deposits with weaker signatures (Type 1 olivine) are distributed in extended deposits in Capri Chasma, West of Ganges Chasma, and Juventae Chasma (mapped in blue to
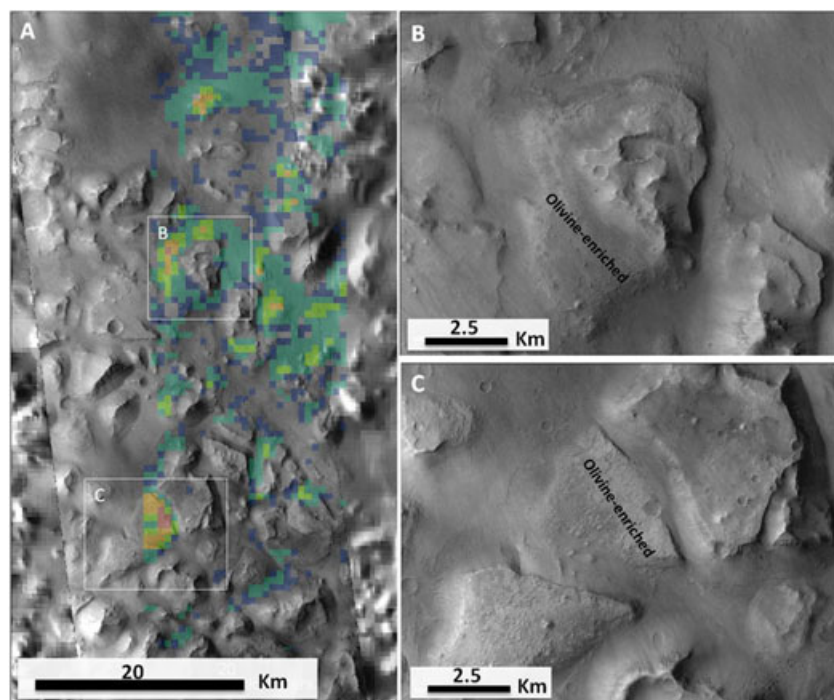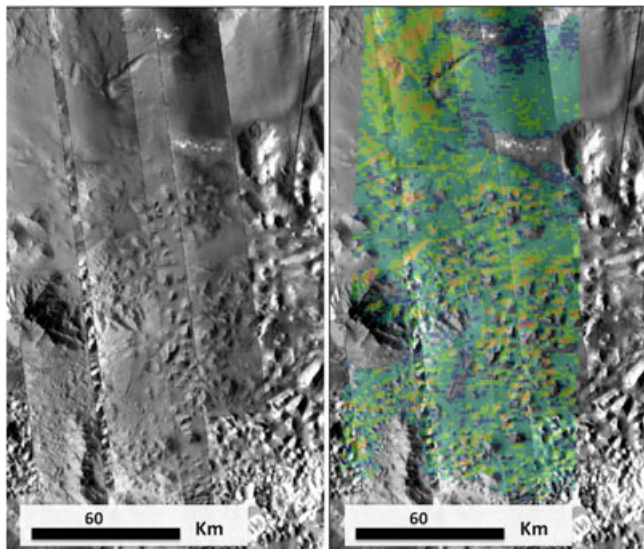

Figure 29. Olivine detections (OSP2 from 1.02 to 1.075) in Aurorae Chaos centered in [–32.2°E, 10.6°S] (A) with two CTX close-ups (B,C) (CTX_ID P12_005912_1703_XN_09S035W).

green in Figure 27A), but they are associated with sand accumulated in the floor instead of bedrock (Figures 27 and 30). In these three regions, the strongest signatures are primarily associated with chaotic terrains. This sand could originate from erosion of local olivine-bearing layer outcrops present under chaotic mounds as in the south of Aurorae Chaos and Hydraotes Chasma. However, such an olivine-bearing layer was not detected by OMEGA, THEMIS, and higher spatial resolution CRISM observations (J. Flahaut, personal communication, 2012), making uncertain the source of the olivine mobile materials.

4.4.2. Origin and Implication

[74] Olivine-bearing terrains found in the chaotic terrains of Aurorae Chaos, Eos, and East of Ganges Chasmata and Hydratoes Chasma are all associated with outcrops exhibiting the same thermal and morphological properties (high nighttime temperature, high albedo, consolidated nature). Their uppermost surfaces are remarkably exposed in the −3900 to −3600 m elevation range. These observations suggest that these outcrops are part of an olivine-bearing layer present at this elevation, widespread over Aurorae Chaos and Eos and Ganges Chasmata as previously reported by *Edwards et al.* [2008]. Some of these outcrops are buried under olivine-poor material, indicating that this layer has been covered by an olivine-poor layer in some areas. A careful study conducted by *Edwards et al.* [2008] of the layer dip angle and the dip azimuth of the Valles Marineris plateau surface and of the olivine layer, suggests that several regional tectonic events have affected the stratigraphic column, or that deposition of the olivine-bearing layer may have occurred on an inclined surface. The extent of this olivine-bearing layer was estimated at a maximum to about $6.6 \times 10^5 \, \text{km}^2$ [*Edwards et al.*, 2008], but the detection by OMEGA of new outcrops at the south of Eos Chasma as well as the presence of olivine-bearing sand deposits in Capri, Ganges, and Juventae Chasmata, which could result from erosion of bedrock, lead to the possibility that olivine-bearing outcrops may be more widespread in the Valles Marineris canyon system.

[75] Several origins have been discussed to account for olivine-bearing extended layer in the Valles Marineris canyon [*Edwards et al.*, 2008]. The favored one is picritic lava flows related to the initiation of the Tharsis volcanism in the early to middle Noachian and subsequently buried by more evolved and fractionated olivine depleted lavas. Similar explanations have been proposed for Syrtis Major and the Isidis basin regions where Noachian to Hesperian picritic lavas were erupted in the early stage of volcanism at Syrtis Major [*Tornabene et al.*, 2008]. Our analysis cannot rule out this scenario. However, the global view of olivine-bearing deposits spread over a variety of Mars units, derived from our study, advocates for a common origin for the emplacement of most of them, including those located within Valles Marineris; it would be related to a global event of olivine-enriched volcanism, which occurred during the early Hesperian and has filled the northern plains and numerous craters and intercrater plains of the southern highlands. In addition, the Ganges and Eos Chasmata layer unit is relatively close (~1500 km) to the near-surface olivine-bearing layer identified in Chryse Planitia (section 4.3) and crops out at a similar elevation, which may indicate a common origin.
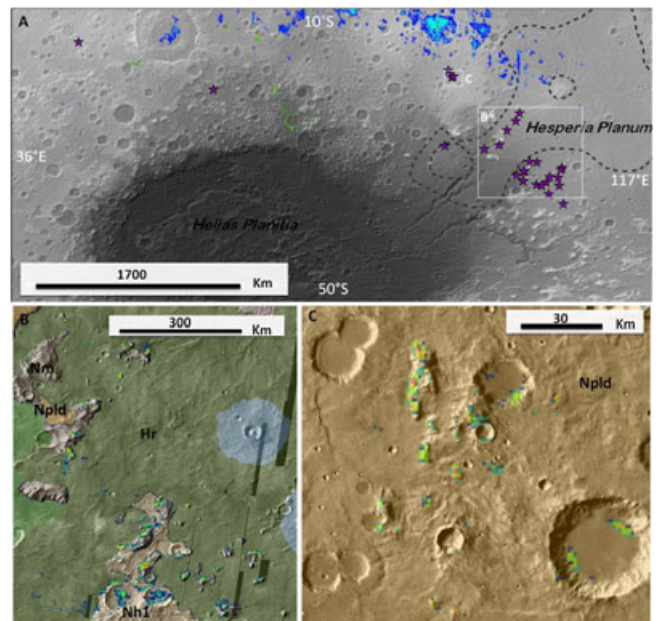
Figure 31. (A) Map of olivine-bearing outcrops surrounding Hellas basin. (B) Close-up of olivine detections (OSP2 from 0.98 to 1.02) centered in [103.5°E, 27.5°S] on geological USGS global map [*Skinner et al.*, 2006] (Green unit: Hesperian ridged plains material (Hr); Brown units: Noachian units: (Nh1) Hellas Basin-rim unit; (Npld) plateau sequence, dissected unit; (Nm) Mountainous material). The outcrops are located in (Nm) unit referred to as ancient crustal material uplifted during formation of impact basins. (C) Other detections (OSP2 from 0.975 to 1.0) found in Noachian unit (brown color) centered in [92.6°E, 19.7°S] with similar morphology.

Figure 30. Olivine detections in Capri Chasma (OSP2 from 1 to 1.035) centered on [−48.8°E, 16°S] (CTX_ID from left to right P12_005912_1703_XN_09S035W, P12_005662_1653_XN_14S049W, P18_008088_1652_XN_14S049W, P11_005451_1663_XN_13S049W). Olivine is primarily associated with sandy deposits.

4.5. Noachian Olivine-bearing Outcrops

[76] In the southern highlands, olivine is also found associated with very rugged, isolated blocks mostly around the Hellas basin outside of the basin terrace (Figure 31). Most of them are located in the eastern outer edges of the Hellas terrace exclusively on Noachian unit named "mountainous material" (Nm) [*Skinner et al.*, 2006]. This unit is interpreted to be most ancient crustal material uplifted during formation of impact basins [*Skinner et al.*, 2006], and is surrounded by Hesperian Hesperia Planum ridged plains (Figure 31B). Other olivine-bearing outcrops were found in three locations in the northeast, north, and northwest of Hellas basin (Figure 31C). These outcrops are found in Noachian units (Npld) [*Skinner et al.*, 2006] and they are morphologically similar to those identified as very ancient mountainous material (Nm), suggesting that they could also constitute uplifted crustal material. As for olivine-bearing hills on the Hellas and Argyre terraces (discussed in section 4.2), olivine signatures are well correlated with the warmer nighttime temperature terrains of outcrops, which mainly corresponds to slopes where bedrock is exposed. The ratioed technique is in favor of olivine type 2.

[77] All olivine-bearing outcrops were found in Noachian units in the vicinity (< 2000 km) of the Hellas basin, which supports their relationship with its formation [*Skinner et al.*, 2006]. These deposits are the only evidence for olivine-bearing material of primitive or Noachian age in the southern highlands detected with OMEGA. Some other evidences were found with CRISM data, which detect olivine in central peaks of some craters of the southern highlands, interpreted to be excavated crustal Noachian rock [*Skok et al.*, 2012]. These observations, in addition to the olivine-bearing deposits found in large craters of northern plains (section 4.3), support the idea that the oldest (earliest) Noachian crust contains olivine at least regionally.

5. Summary and Perspectives

[78] The main results of this study are summarized in Figure 32. For each major geological setting, the major observations, conclusions, and interpretations are presented in the specific sections 4.1.4 (smooth crater floors and flat plains), 4.2.3 (circum-Argyre and -Hellas basins), 4.3.2 (Northern plains), 4.4.2 (Valles Marineris), and 4.5 (Noachian olivine outcrops).

[79] One of the major outcomes of our study is that olivine is found associated with ancient (early) Noachian crustal rock (sections 4.3 and 4.5) and to early Hesperian volcanism (section 4.1); by contrast, it is not detected in later Noachian terrains, which cover the major part of the southern highlands. This could reflect a difference in the composition of the parent rocks, with middle to late Noachian material deriving from olivine-poor bedrock relative to early Noachian
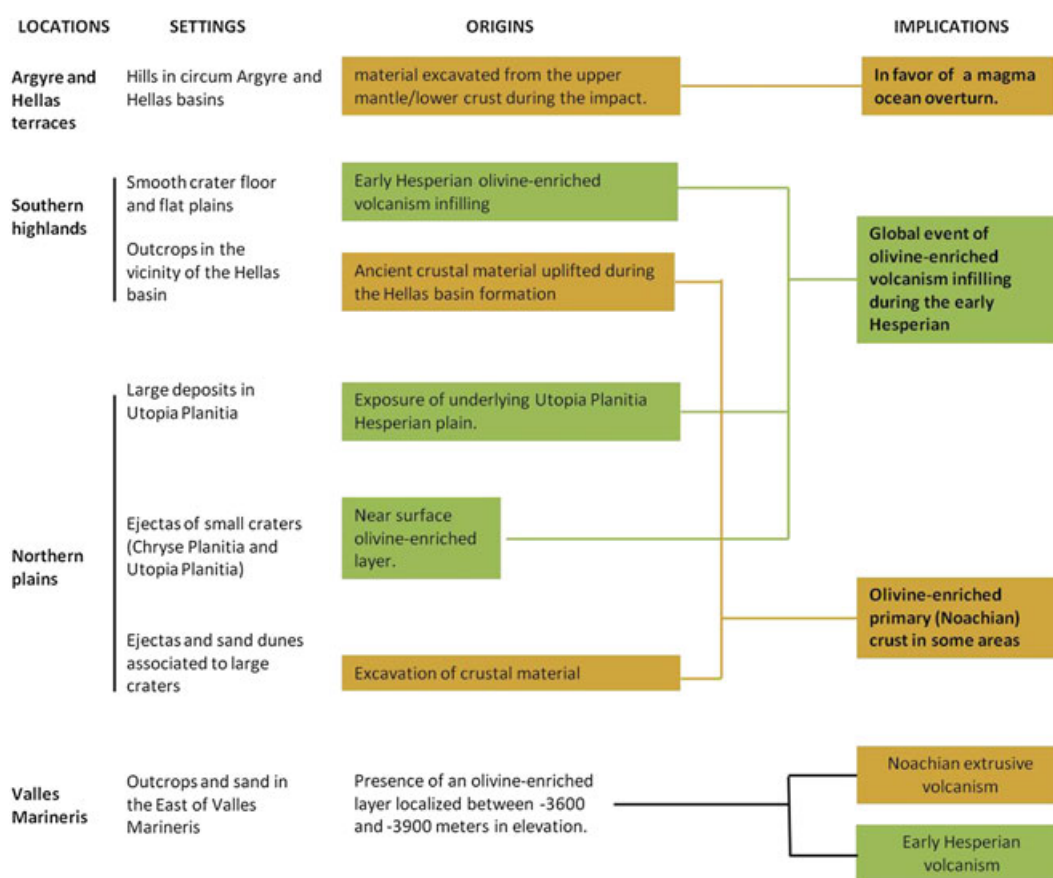

Figure 32. Main characteristics of olivine-bearing settings. Brown and green squares are related to Noachian and early Hesperian epochs, respectively.

and Hesperian units. A tentative explanation by *Bandfield et al.* [2011], as mentioned in section 4.1, would account for the low content of olivine in the ancient soils by its dissolution through deep aqueous alteration. However, the absence of olivine signature in sediments, eroded terrains or crater ejecta in the Noachian southern highlands soil argue against their being previously olivine-bearing and thus favors an explanation coupling the variation in olivine, from early Noachian to Amazonian terrains, to that of the pristine bedrock formed along Mars History. The olivine enrichment of the Hesperian lavas in comparison to Noachian terrains could result from an evolution of mantle temperature; a cooling during the mid-to-late Noachian preventing the crystallization of olivine followed by an increase of the temperature during early Hesperian, which initiated partial melting sufficiently important to form olivine-enriched lavas. This thermal evolution could be due to the heat-producing elements such as uranium and thorium. Such a scenario was proposed and successfully simulated for the formation of lunar mare volcanism [*Wieczorek and Phillips*, 2000]. These results would thus constitute a strong set of constraints to the magmatic and volcanic evolution of Mars.

[80] Of specific and critical significance is the limited duration, from 3.8 to 3.6 Ga typically, of the volcanic event responsible for the infilling of olivine-bearing lava throughout the planet, from which most olivine-bearing spots we identified are originating. *Head et al.* [2002] estimated the surface coverage of volcanic plains, including the Hesperian-aged ridged plains underlying the northern lowlands; they found a value of 43×10^6 km^2, similar to that of *Tanaka et al.* [1988, 1992]. We show that numerous smooth crater floors and flat plains previously mapped as Noachian-aged units [*Tanaka et al.*, 1988, 1992; *Skinner et al.*, 2006] are likely related to this early Hesperian volcanism. An estimate of the total Martian surface resurfaced by this volcanism, including new Early Hesperian olivine-bearing units mapped in this investigation, with a better knowledge of magma composition, will also lead to a significant increase of the gas and volatiles peak input into the atmosphere during the Early Hesperian.

[81] This study also demonstrates that NIR hyperspectral imagery is a powerful technique to study the presence of olivine on Mars; however, its spectral variations are difficult to interpret in terms of iron content, abundance and grain size. For instance, Type 1 olivine could have similar iron content than Type 2 at local scale, the difference of spectral signature being then due to grain size effect and/or abundance effects. Integrating both thermal, near-infrared and visible data sets to discriminate between iron content, grain size, and abundance effects, would be thus needed to better determine the olivine composition. Comparing olivine composition between different olivine-bearing settings throughout the Martian surface (such as Hesperian and Noachian deposits, southern highlands and northern plains Hesperian deposits, Valles Marineris and Chryse Planitia deposits) would validate the proposed evolution with time of Mars activity.

References

Bandfield, J. L. (2002), Global mineral distributions on Mars, *J. Geophys. Res.*, *107*(E6), 5042, doi:10.1029/2001JE001510.

Bandfield, J. L., and A. D. Rogers (2008), Olivine dissolution by acidic fluids in Argyre Planitia, Mars: Evidence for a widespread process?, *Geology*, *36*, 579–582

Bandfield, J. L., A. D. Rogers, and C. S. Edwards (2011), The role of aqueous alteration in the formation of martian soils, *Icarus*, *211*, 157–171, doi: 10.1016/j.icarus.2010.08.028

Bibring, J.-P., et al. (2004), OMEGA: Observatoire pour la Minéralogie, l'Eau, les Glaces et l'Activité, in *Mars Express; The Scientific Payload,* edited by Andrew Wilson, pp. 37– 49, ESA Publication Division, ESTEC, Noordwijk, Netherlands.

Bibring, J.-P., et al. (2005), Mars surface diversity as revealed by the OMEGA/Mars Express observations, *Science*, *307*, 1576–1581, doi:10.1126/science.1109509.

Bishop, J. L. et al. (2012), Mineralogy and morphology of geologic units at Libya Montes, Mars: Ancient aqueously derived outcrops, mafic flows, fluvial features and impacts, *J. Geophys. Res.*, doi:10.1029/2012JE004151, in press.

Carrozzo, F. G., F. Altieri, G. Bellucci, F. Poulet, E. D'Aversa, and J.-P. Bibring (2012), Iron mineralogy of the surface of Mars from the 1 μm band spectral properties, *J. Geophys. Res.*, *117*, E00J17, doi: 10.1029/2012JE004091.

Carter, J., F. Poulet, J.-P. Bibring, and S. Murchie (2010), Detection of Hydrated Silicates in Crustal Outcrops in the Northern Plains of Mars, *Science*, *328*, 1682–1686, doi: 10.1126/science.1189013

Christensen, P. R. (1986), The spatial distribution of rocks on Mars, *Icarus*, *68*, 217–238, doi: 10.1016/0019-1035(86)90020-5

Christensen, P. R., and H. J. Moore (1992), The martian surface layer, in *Mars edited by H. H. Kieffer et al., pp. 686–729, Univ. Arizona Press, Tucson.*

Christensen, P. R., et al. (2003), Morphology and composition of the surface of Mars: Mars Odyssey THEMIS results, *Science*, *300*, 2056–2061, doi: 10.1126/science.1080885

Christensen, P. R., et al. (2005), Evidence for magmatic evolution and diversity on Mars from infrared observations, *Nature*, *436*, 504–509, doi: 10.1038/nature03639

Debaille, V., and A. D. Brandon (2011), Mantle overturn as revealed by Nakhlites: What happened after, paper presented at 74th Meteoritical Soc. Meet., abstract 5310.

Edwards, C. S., P. R. Christensen, and V. E. Hamilton (2008), Evidence for extensive olivine-rich basalt bedrock outcrops in Ganges and Eos chasmas, Mars, *J. Geophys. Res.*, *113*, E11003, doi:10.1029/2008JE003091

Edwards, C. S., J. L. Bandfield, P. R. Christensen, and R. L. Fergason (2009), Global distribution of bedrock exposures on Mars using THEMIS high-resolution thermal inertia, *J. Geophys, Res.*, *114*, E11, doi: 10.1029/2009JE003363

Edwards, C. S., and P. R. Christensen (2011), Evidence for a Widespread Olivine-Rich Layer on Mars: Identification of a Global Impact Ejecta Deposit?, paper presented at 42nd Lunar Planet. Sci. Conf., The Woodlands, Texas. LPI Contribution No. 1608, p.2560

Elkins-Tanton, L. T., N. Chatterjee, and T. L. Grove (2003), Magma ocean fractional crystallization and cumulate overturn in terrestrial planets: Implications for Mars, *Meteoritics Planet Sci.*, *38*, 1753–1771, doi: 10.1111/j.1945-5100.2003.tb00013.x

Elkins-Tanton, L. T., P. C. Hess, and E. M. Parmentier (2005), Possible formation of ancient crust on Mars through magma ocean processes, *J. Geophys. Res.*, *110*, E12, doi: 10.1029/2005JE002480

Fergason, R. L., P. R. Christensen, J. F. Bell III, M. P. Golombek, K. E. Herkenhoff, and H. H. Kieffer (2006), Physical properties of the Mars Exploration Rover landing sites as inferred from Mini-TES derived thermal inertia, *J. Geophys. Res*, *111*, doi:10.1029/2005JE002583.

Gaffey, S. J., L. A. McFadden, D. Nash, and C. Pieters (1993), Ultraviolet, visible and near-infrared reflectance spectroscopy: Laboratory spectra of geologic materials, in *Remote Geochemical Analysis: Elemental and Mineralogical Composition, edited by C. Pieters and P. A. J. Englert, pp. 43– 77, Cambridge Univ. Press, New York.*

Gomes, R., H. F. Levison, K. Tsiganis, and A. Morbidelli (2005), Origin of the cataclysmic Late Heavy Bombardment period of the terrestrial planets, *Nature*, *435*, 466–469

Goudge, T. A., J. F. Mustard, J. W. Head, and C. I. Fassett (2011), Open-Basin Lakes on Mars: A Study of Mineralogy Along a Paleolake Chain, paper presented at 42nd Lunar Planet. Sci. Conf., The Woodlands, Texas. LPI Contribution No. 1608, p.2244.

Greeley, R., and B. D. Schneid (1991), Magma generation on Mars - Amounts, rates, and comparisons with earth, moon, and Venus, *Science*, *254*, 996–998, doi: 10.1126/science.254.5034.996

Greeley, R., and M. Kraft (2001), Survivability of aggregate sands on Mars, Lunar Planet. Sci., 32, abstract #1839.

Hamilton, V. E., and P. R. Christensen (2005), Evidence for extensive, olivine-rich bedrock on Mars, *Geology*, *33*, 433– 436, doi:10.1130/G21258.1

Hamilton, V. E., M. L. McDowell, and W. C. Koeppen (2010), Correlations between olivine abundance and thermal inertia: Implications for global

weathering and/or alteration on Mars, Lunar Planet. Sci., 41, abstract #1533.

Hartmann, W. K., and G. Neukum (2001), Cratering Chronology and the Evolution of Mars, *Space Sci. Rev.*, *96*, 165–194

Head, J. W., M. A. Kreslavsky, A. Mikhail, and S. Pratt (2002), Northern lowlands of Mars: Evidence for widespread volcanic flooding and tectonic deformation in the Hesperian Period, *J. Geophys. Res.*, *107*, E1, doi: 10.1029/2000JE001445

Hiesinger, H., J. W. Head III, U. Wolf, R. Jaumann, and G. Neukum (2003), Ages and stratigraphy of mare basalts in Oceanus Procellarum, Mare Nubium, Mare Cognitum, and Mare Insularum, *J. Geophys. Res.*, *108*, 5065, doi: 10.1029/2002JE001985

Hoefen, T. M., R. N. Clark, J. L. Bandfield, M. D. Smith, J. C. Pearl, and P. R. Christensen (2003), Discovery of olivine in the Nili Fossae region of Mars, *Science*, *302*, 627–630, doi:10.1126/science.1089647

Ivanov, B. A. (2001), Mars/Moon Cratering Rate Ratio Estimates, *Space Sci. Rev.*, *96*, 87–104.

Jakosky, B. M., and P. R. Christensen (1986), Global duricrust on Mars: Analysis of remote-sensing data, *J. Geophys. Res.*, *91*, 3547–3559, doi: 10.1029/JB091iB03p03547

Jaumann, R., et al. (2007), The high-resolution stereo camera (HRSC) experiment on Mars Express: Instrument aspects and experiment conduct from interplanetary cruise through the nominal mission, *Planet. Space Sci.*, *55*, 928–952, doi: 10.1016/j.pss.2006.12.003

Kieffer, H. H., T. Z. Martin, A. R. Peterfreund, B. M. Jakosky, E. D. Miner, and F. D. Palluconi (1977), Thermal and albedo mapping of Mars during the Viking primary mission, *J. Geophys, Res.*, *82*, 4249–4291, doi: 10.1029/JS082i028p04249

Koeppen W. C., and V. E. Hamilton (2008), Global distribution, composition, and abundance of olivine on the surface of Mars from thermal infrared data, *J. Geophys. Res.*, *113*, E05001, doi: 10.1029/2007JE002984

Lane, M. D., and C. A. Goodrich (2010), High-Magnesian Olivine in the Argyre Rim: Derived from a Primitive Magma?, paper presented at 41st Lunar Planet. Sci. Conf., The Woodlands, Texas. LPI Contribution No. 1533, p.2094.

Langevin, Y., J.-P. Bibring, F. Montmessin, F. Forget, M. Vincendon, S. Douté, F. Poulet, and B. Gondet (2007), Observations of the south seasonal cap of Mars during recession in 2004– 2006 by the OMEGA visible/near-infrared imaging spectrometer on board Mars Express, *J. Geophys. Res.*, doi:10.1029/2006JE002841

Leverington, D. W. (2004), Volcanic Resurfacing as an Alternative Mechanism for Formation of Martian "Crater Lake" Features, American Geophysical Union, spring Meeting, abstract #P33D-08.

Loizeau, D., J. Carter, S. Bouley, N. Mangold, F. Poulet, J.-P. Bibring, F. Costard, Y. Langevin, B. Gondet, and S. L. Murchie (2012), Characterization of hydrated silicate-bearing outcrops in Tyrrhena Terra, Mars: Implications to the alteration history of Mars, *Icarus*, *219*, 476–497, doi: 10.1016/j.icarus.2012.03.017

Malin, M. C., et al. (2007), Context Camera Investigation on board the Mars Reconnaissance Orbiter, *J. Geophys. Res.*, *112*, E5, doi: 10.1029/2006JE002808

Mangold, N., D. Baratoux, O. Arnalds, J.-M. Bardintzeff, B. Platevoet, M. Gregoire, and P. Pinet (2011), Segregation of olivine grains in volcanic sands in Iceland and implications for Mars, *Earth Planet. Sci. Lett.*, *310*, 233–243.

McEwen, A. S., et al. (2007), Mars Reconnaissance Orbiter's High Resolution Imaging Science Experiment (HiRISE), *J. Geophys. Res.*, *112*, E5, doi: 10.1029/2005JE002605

McSween, H. Y., et al. (2006), Characterization and petrologic interpretation of olivine-rich basalts at Gusev Crater, Mars, *J. Geophys. Res.*, *111*, E02S10, doi: 10.1029/2005JE002477.

McSween, H. Y., G. J. Taylor, and M. B. Wyatt (2009), Elemental Composition of the Martian Crust, *Science*, *324*, 736–739, doi:10.1126/science.1165871

Mellon, M. T., B. M. Jakosky, H. H. Kieffer, and P. R. Christensen (2000), High resolution thermal inertia mapping from the Mars Global Surveyor Thermal Emission Spectrometer, *Icarus*, *148*, 437–455, doi:10.1006/icar.2000.6503

Michael, G. G., and G. Neukum (2010), Planetary surface dating from crater size-frequency distribution measurements: Partial resurfacing events and statistical age uncertainty, *Earth Planet. Sci. Lett.*, *294*, 223–229

Mustard, J. F., F. Poulet, A. Gendrin, J.-P. Bibring, Y. Langevin, B. Gondet, N. Mangold, G. Bellucci, and F. Altieri (2005), Olivine and pyroxene diversity in the crust of Mars, *Science*, *307*, 1594–1597, doi:10.1126/science.1109509.

Mustard, J. F., F. Poulet, J. W. Head, N. Mangold, J.-P. Bibring, S. M. Pelkey, C. I. Fassett, Y. Langevin, and G. Neukum (2007), Mineralogy of the Nili Fossae region with OMEGA/Mars Express data: 1. Ancient impact melt in the Isidis Basin and implications for the transition from the Noachian to Hesperian, *J. Geophys. Res.*, *112*, E8, doi: 10.1029/2006JE002834

Mustard, J. F., B. L. Ehlmann, S. L. Murchie, F. Poulet, N. Mangold, J. W. Head, J.-P. Bibring, and L. H. Roach (2009), Composition, Morphology, and Stratigraphy of Noachian Crust around the Isidis basin, *J. Geophys. Res.*, *114*, E00D12, doi: 10.1029/2009JE003349

Nemchin, A., N. Timms, R. Pidgeon, T. Geisler, S. Reddy, and C. Meyer (2009), Timing of crystallization of the lunar magma ocean constrained by the oldest zircon, *Nature Geo.*, *2*, 133–136.

Ody, A., F. Poulet, Y. Langevin, J.-P. Bibring, G. Bellucci, F. Altieri, B. Gondet, M. Vincendon, and J. Carter (2012), Global maps of anhydrous mineral at the surface of Mars from OMEGA/Mex, *J. Geophys. Res.*, doi:10.1029/2012JE004117.

Palluconi, F. D., and H. H. Kieffer (1981), Thermal inertia mapping of Mars from 60∘ S to 60∘ N, *Icarus*, *45*, 415–426.

Pelkey, S. M., B. M. Jakosky, and M. T. Mellon (2001), Thermal inertia of crater-related windstreaks on Mars, *J. Geophys. Res.*, *106*, E10, doi:10.1029/2000JE001433.

Poulet, F., and S. Erard (2004), Nonlinear spectral mixing: Quantitative analysis of laboratory mineral mixtures, *J. Geophys. Res.*, *109*, E02009, doi:10.1029/2003JE002179.

Poulet, F., C. Gomez, J.-P. Bibring, Y. Langevin, B. Gondet, P. Pinet, G. Bellucci, and J. Mustard (2007), Martian surface mineralogy from Observatoire pour la Minéralogie, l'Eau, les Glaces et l'Activité on board the Mars Express spacecraft (OMEGA/MEx): Global mineral maps, *J. Geophys. Res.*, *112*, E08S02, doi: 10.1029/2006JE00284.

Poulet, F., Y. Langevin, G. Boubin, D. Jouglet, J.-P. Bibring, and B. Gondet (2008), Spectral variability of the Martian high latitude surfaces, *Geophys. Res. Lett.*, *35*, L20201, doi: 10.1029/2008GL035450

Poulet, F., J.-P. Bibring, Y. Langevin, J. F. Mustard, N. Mangold, M. Vincendon, B. Gondet, P. Pinet, J.-M. Bardintzeff, and B. Platevoet (2009a), Quantitative compositional analysis of martian mafic regions using the MEx/OMEGA reflectance data 1. Methodology, uncertainties and examples of application, *Icarus*, *201*, 69–83, doi: 10.1016/j.icarus.2008.12.025

Poulet, F., N. Mangold, B. Platevoet, J.-M. Bardintzeff, V. Sautter, J. F. Mustard, J.-P. Bibring, P. Pinet, Y. Langevin, B. Gondet, and A. Aléon-Toppani (2009b), Quantitative compositional analysis of martian mafic regions using the MEx/OMEGA reflectance data. 2. Petrological implications, *Icarus*, *201*, 84–101, doi: 10.1016/j.icarus.2008.12.042

Putzig, N. E., and M. T. Mellon (2007), Apparent thermal inertia and the surface heterogeneity of Mars, *Icarus*, *191*, 68–94, doi: 10.1016/j.icarus.2007.05.013

Rogers, A. D. , and P. R. Christensen (2003), Age relationship of basaltic and andesitic surface compositon on Mars: Analysis of high-resolution TES observation of the northern hemisphere, *J. Geophys, Res.*, doi:10.1029/2002JE001913.

Rogers, A. D., O. Aharonson, and J. L. Bandfield (2009), Geologic context of in situ rocky exposures in Mare Serpentis, Mars: Implications for crust and regolith evolution in the cratered highlands, *Icarus*, *200*, 446–462, doi: 10.1016/j.icarus.2008.11.026

Rogers, A. D., P. R. Christensen, and J. L. Bandfield (2005), Compositional heterogeneity of the ancient Martian crust: Analysis of Ares Vallis bedrock with THEMIS and TES data, *J. Geophys. Res.*, *110*, Eo5010, doi: 10.1029/2005JE002399.

Rogers, A. D., and R. L. Fergason (2011), Regional-scale stratigraphy of surface units in Tyrrhena and Iapygia Terrae, Mars: Insights into highland crustal evolution and alteration history, *J. Geophys. Res.*,*116*, E8, doi: 10.1029/2010JE003772

Ruff, S. W., A. S. McEwen, and Athena Science Team (2007), An Emerging View of the Stratigraphy of the Columbia Hills in Gusev Crater from HiRISE and Mini-TES Data, paper presented at 38th Lunar Planet. Sci. Conf., League City, Texas. LPI Contribution No. 1338, p.2063.

Salvatore, M. R., J. F. Mustard, M. B. Wyatt, and S. L. Murchie (2010), Definitive evidence of Hesperian basalt in Acidalia and Chryse planitiae, *J. Geophys. Res.*, *115*, E7, doi: 10.1029/2009JE003519

Schultz, P. H., and P. D. Spudis (1983), the beginning and end of mare volcanism on the moon, paper presented at 14th Lunar Planet. Sci. conf., Houston, Texas, p. 676–677.

Sharp, R. P. (1973), Mars: Fretted and Chaotic Terrains, *J. Geophys. Res.*, *78*, 4073–4083.

Shkuratov, Y., L. Starukhina, H. Hoffmann, and G. Arnold (1999), A model of spectral albedo of particulate surfaces: Implications for optical properties of the moon, *Icarus*, *137*, 235–246.

Skinner, J. A., Jr., T. M. Hare, and K. L. Tanaka (2006), Digital Renovation of the Atlas of Mars 1:15,000,000-Scale Global Geologic Series Maps, paper presented at 37th Lunar Planet. Sci. Conf., League City, Texas, abstract no.2331.

Skok, J. R., Mustard, J. F., Tornabene, L. L., Pan, C., Rogers, D., and S. L. Murchie. (2012), A Spectroscopic Analysis of Martian Crater Central

Peaks: Formation of the Ancient Crust. *J. Geophys. Res.*, *117*, E00J18, doi: 10.1026/2012JE004148

Stewart, S. T. (2011), Impact Basin Formation: The Mantle Excavation Paradox Resolved, paper presented at 42nd Lunar Planet. Sci. Conf. 42nd, The Woodlands, Texas. LPI Contribution No. 1608, p.1633.

Tanaka, K. L., N. K. Isbell, D. H. Scott, R. Greeley, and J. E. Guest (1988), The resurfacing history of Mars - A synthesis of digitized, viking-based geology, proceeding of 18th Lunar Planet. Sci. Conf., Houston, Texas, p. 665–678.

Tanaka, K. L., D. H. Scott, and R. Greeley (1992), Global stratigraphy, in *Mars*, edited by H. H. Kieffer, et al., pp. 345–382, Univ. Arizona Press, Tucson.

Taylor, S. R., and McLennan, S. M. (2009), *Planetary Crusts: Their Composition, Origin, and Evolution*. Cambridge University Press, Cambridge.

Tirsch, D., R. Jaumann, A. Pacifici, F. Poulet, L. H. Roach, J. F. Mustard, J.-P. Bibring, and G. Neukum (2009), paper presented at 40th Lunar Planet. Sci. Conf., The Woodlands, Texas, id.1004.

Tornabene, L. L., J. E. Moersch, H. Y. McSween, V. E. Hamilton, J. L. Piatek, and P. R. Christensen (2008), Surface and crater-exposed lithologic units of the Isidis Basin as mapped by coanalysis of THEMIS and TES derived data product, *J. Geophys. Res.*, *113*, E10, doi: 10.1029/2007JE002988.

Warren, P. H. (1985), The magma ocean concept and lunar evolution, in *Annual Review of Earth and Planetary Sciences, Vol 13*, p. 201–240, Palo Alto, CA.

Werner, S. C. (2009), The global martian volcanic evolutionary history, *Icarus*, *201*, 44–68.

Wieczorek, M., and R. Phillips (2000), The "Procellarum KREEP Terrane": Implications for mare volcanism and lunar evolution, *J. Geophys. Res.*, *105*, E8, doi:10.1029/1999JE001092

Williams, D. A., R. Greeley, L. Manfredi, J. Raitala, and G. Neukum (2010), The Circum-Hellas Volcanic Province, Mars: Assessement of wrinkle-ridged plains, *Earth Planet. Sci. Lett.*, *294*, 492–505.